

# A numerical study on the turbulence characteristics in an air–water upward bubbly pipe flow

Ingu Lee<sup>1</sup>, Jaehee Chang<sup>1</sup>, Kiyoun Kim<sup>1</sup> and Haechon Choi<sup>1,2,†</sup>

<sup>1</sup>Department of Mechanical Engineering, Seoul National University, Seoul 08826, Korea

<sup>2</sup>Institute of Advanced Machines and Design, Seoul National University, Seoul 08826, Korea

(Received 2 August 2023; revised 28 June 2024; accepted 29 June 2024)

A high-resolution numerical simulation of an air–water turbulent upward bubbly flow in a pipe is performed to investigate the turbulence characteristics and bubble interaction with the wall. We consider three bubble equivalent diameters and three total bubble volume fractions. The bulk and bubble Reynolds numbers are  $Re_{bulk} = u_{bulk}D/\nu_w = 5300$  and  $Re_{bub} = (\langle u_{bub} \rangle - u_{bulk})d_{eq}/\nu_w = 533\text{--}1000$ , respectively, where  $u_{bulk}$  is the water bulk velocity,  $\langle u_{bub} \rangle$  is the overall bubble mean velocity,  $D$  is the pipe diameter and  $\nu_w$  is the water kinematic viscosity. The mean water velocity near the wall significantly increases due to bubble interaction with the wall, and the root-mean-square water velocity fluctuations are proportional to  $\bar{\psi}(r)^{0.4}$ , where  $\bar{\psi}(r)$  is the mean bubble volume fraction. For the cases considered, the bubble-induced turbulence suppresses the shear-induced turbulence and becomes the dominant flow characteristic at all radial locations including near the wall. Rising bubbles near the wall mostly bounce against the wall rather than slide along the wall or hang around the wall without collision. Low-speed streaks observed in the near-wall region in the absence of bubbles nearly disappear due to the bouncing bubbles. These bouncing bubbles generate counter-rotating vortices in their wake, and increase the skin friction by sweeping high-speed water towards the wall. We also suggest an algebraic Reynolds-averaged Navier–Stokes model considering the interaction between shear-induced and bubble-induced turbulence. This model provides accurate predictions for a wide range of liquid bulk Reynolds numbers.

**Key words:** gas/liquid flow, pipe flow, turbulence simulation

† Email address for correspondence: [choi@snu.ac.kr](mailto:choi@snu.ac.kr)

© The Author(s), 2024. Published by Cambridge University Press. This is an Open Access article, distributed under the terms of the Creative Commons Attribution licence (<http://creativecommons.org/licenses/by/4.0>), which permits unrestricted re-use, distribution and reproduction, provided the original article is properly cited.

## 1. Introduction

Wall-bounded liquid flows containing bubbles have received much attention because of their importance in various industrial fields such as chemical reactors (Hibiki & Ishii 2002) and nuclear plants (Krepper, Lucas & Prasser 2005). Due to the buoyancy of bubbles, the flow characteristics of bubbly flows depend on the angle between the directions of the buoyancy force and mean liquid flow. Among others, upward bubbly flow has been the subject of extensive research to gain insight into the dynamics of bubbles and their impact on various liquid flow characteristics, including turbulence, heat transfer and mixing.

The characteristics of wall-bounded upward bubbly flow in a pipe or channel are known to significantly depend on the wall-normal distribution of bubbles such as the core-peaking and wall-peaking bubble distributions. The former has a linear profile of the Reynolds shear stress around the centre, while the latter has a concave profile around the centre with a nearly uniform mean velocity except near the wall (Colin, Fabre & Kamp 2012; Dabiri, Lu & Tryggvason 2013; Du Cluzeau, Bois & Toutant 2019). Besides, the wall-peaking bubble distribution provides a higher skin friction than that of single-phase flow at the same liquid bulk velocity (Moursali, Marié & Bataille 1995; Liu 1997). One of the most important factors of determining the bubble distribution is the direction of the shear-induced lift force. Saffman (1965) showed that a spherical object travelling along the mean flow direction in a shear flow experiences a lateral lift force towards the maximum relative velocity to the object velocity. However, early experiments (Sekoguchi, Sato & Honda 1974; Liu & Bankoff 1993) on upward bubbly pipe flows revealed that bubbles larger than a critical diameter were predominantly located in the middle, which is contrary to the result of Saffman (1965), and thus this phenomenon is called the lift force reversal. Tomiyama *et al.* (2002) examined the force acting on a single bubble in a shear flow and concluded that a modified Eötvös number,  $Eo = \rho_l g l_{bub}^2 / \sigma$ , is the main parameter to determine the direction of the lift force, where  $\rho_l$  is the liquid density,  $g$  is the gravitational acceleration,  $l_{bub}$  is the major axis of an ellipsoidal bubble and  $\sigma$  is the surface tension coefficient. Dabiri *et al.* (2013) also suggested that the bubble deformability is a crucial factor in determining the bubble distribution in a bubbly channel flow. Adoua, Legendre & Magnaudet (2009) explained the mechanism of the lift force reversal on a spheroidal bubble by observing the changes in the rotational direction of the vortices in the wake.

The turbulence characteristics of an upward bubbly pipe flow are affected by two different fluctuations that come from the wall shear and buoyant bubbles. They are referred to as shear-induced turbulence and bubble-induced turbulence (or pseudo-turbulence), respectively, and the characteristics of bubble-induced turbulence have been investigated through studies on rising gas bubbles in a stagnant liquid. Owing to bubble-induced turbulence, the spectral densities of the liquid velocity fluctuations follow the power of  $-3$  slope, i.e.  $E(f) \sim f^{-3}$  and  $E(k) \sim k^{-3}$  (Riboux, Risso & Legendre 2010; Roghair *et al.* 2011), and the root-mean-square (r.m.s.) velocity fluctuations are proportional to  $\langle \psi \rangle^{0.4}$  (Risso & Ellingsen 2002; Riboux *et al.* 2010), where  $f$  is the frequency,  $k$  is the wavenumber and  $\langle \psi \rangle$  is the total bubble volume fraction. These results were examined in the presence of background isotropic turbulence by Prakash *et al.* (2016) and Alm  ras *et al.* (2017). When the background turbulence intensity is larger than a threshold value, the velocity fluctuations change to be proportional to  $\langle \psi \rangle^{1.3}$  (Alm  ras *et al.* 2017), while  $E(f) \sim f^{-3}$  is still maintained (Prakash *et al.* 2016). Riboux, Legendre & Risso (2013) and Amoura *et al.* (2017) decomposed bubble-induced turbulence into the mean and fluctuating velocity components in a reference frame moving with each bubble, and showed that the scaling of the velocity fluctuations with  $\langle \psi \rangle^{0.4}$  was not observed, but  $E(k)$  was proportional to  $k^{-3}$ . Du Cluzeau *et al.* (2022) analysed the Reynolds stress transport

equation of homogeneous bubbly flow with this decomposition, and showed energy conversion from the mean to fluctuating components. Pandey, Ramadugu & Perlekar (2020) explained that  $k^{-3}$  scaling of the energy spectra came from the balance among the surface tension, kinetic energy and viscous dissipation.

Because of the characteristics of bubble-induced turbulence being distinct from those of shear-induced turbulence, it is important to understand the interaction between them in a wall-bounded bubbly flow. Zhang, Yokomine & Kunugi (2015) demonstrated that the presence of a wall can inhibit bubble-induced turbulence and the existence of bubbles can also suppress shear-induced turbulence, despite an overall enhancement in turbulence. Du Cluzeau *et al.* (2019) showed that shear-induced turbulence is reduced at all wall-normal locations in a bubbly channel flow. However, due to the difficulty in distinguishing and comparing these two types of turbulence, our understanding of their interaction remains limited.

For industrial applications of bubbly flow, various Reynolds-averaged Navier–Stokes (RANS) models have been developed to account for bubble-induced turbulence. Sato, Sadatomi & Sekoguchi (1981*a*) suggested an algebraic RANS model for the turbulent viscosity  $\nu_t$  by a linear combination of shear-induced and bubble-induced turbulence. For one-equation (Kataoka 1995), two-equation (Kataoka & Serizawa 1989; Rzehak & Krepper 2013; Ma *et al.* 2017) and Reynolds stress (Colombo & Fairweather 2015; Du Cluzeau *et al.* 2019) models, bubble-induced production and dissipation terms are added to existing single-phase RANS models (Speziale, Sarkar & Gatski 1991; Spalart & Allmaras 1992; Menter 1994). In addition to these turbulence models, force (Lucas, Krepper & Prasser 2001, 2007) and polydispersity (Liao *et al.* 2015) models have been suggested to predict the bubble distribution in the wall-normal direction. Recently, an up-scaling approach using direct numerical simulation has been conducted for better prediction (Bois 2017; Ma *et al.* 2017; Du Cluzeau *et al.* 2019). Du Cluzeau *et al.* (2019) also showed that surface tension, which was not included in most models, is the strongest force in the wall-normal momentum budget equation. Therefore, a further investigation of surface tension and its interaction with surrounding liquid is necessary.

Although there have been numerous studies on wall-bounded bubbly flows, a comprehensive understanding on the effect of bubbles on liquid flow structures is still lacking. According to different flow conditions, there exist numerous types of bubble behaviours during a bubble–wall interaction (bouncing, sliding and oscillating without collision), bubble–bubble interaction (drafting-kissing-tumbling and merging) and rising without interaction (rectilinear rise, zigzagging and spiralling). To understand the bubble–wall interaction and its effect on the near-wall coherent structures, we perform a high-resolution numerical simulation of an air–water upward bubbly pipe flow. We also examine how the turbulence statistics and skin friction are modified by the bubble size and volume fraction. Finally, we suggest an algebraic RANS model considering the interaction between bubble-induced and shear-induced turbulence from the results of the present numerical simulation. Numerical details are given in § 2. The turbulence statistics, bubble behaviour and near-wall vortical structures are discussed in §§ 3.1 and 3.2, followed by conclusions in § 4.

## 2. Numerical details

### 2.1. Governing equations and numerical method

We simulate an air–water upward bubbly pipe flow in Cartesian coordinates with an immersed boundary method (Yang & Balaras 2006). The governing equations

for two-phase immiscible incompressible flow are the continuity and Navier–Stokes equations:

$$\nabla \cdot \mathbf{u} = 0, \quad (2.1)$$

$$\frac{\partial(\rho \mathbf{u})}{\partial t} + \nabla \cdot (\rho \mathbf{u} \mathbf{u}) = -\Pi \mathbf{k} - \nabla p + \nabla[\mu(\nabla \mathbf{u} + \nabla \mathbf{u}^T)] + (\rho - \langle \rho \rangle) \mathbf{g} + \sigma \kappa \delta \mathbf{n} + \mathbf{f}, \quad (2.2)$$

where  $\mathbf{u}$  is the velocity,  $t$  is the time,  $\Pi (= dP/dx + \langle \rho \rangle g)$  is the sum of the mean pressure gradient and weight of air–water mixture,  $\langle \cdot \rangle$  denotes an average in time and over the whole computational domain,  $\mathbf{k}$  is the unit vector in the axial (upward) direction,  $p$  is the pressure fluctuations,  $\mathbf{g} (= -g\mathbf{k})$  is the gravitational acceleration vector,  $\sigma$  is the surface tension coefficient,  $\kappa$  is the curvature,  $\mathbf{n}$  is the surface-normal vector on the phase interface,  $\delta$  is the delta function (1 at the phase interface and 0 otherwise) and  $\mathbf{f}$  is the momentum forcing to satisfy the no-slip boundary condition on the pipe wall (Yang & Balaras 2006). Note that (2.1) and (2.2) are solved in a periodic domain in the axial direction. Here,  $\rho$  and  $\mu$  are the air–water mixture density and viscosity, respectively, defined as

$$\rho = \rho_a \psi + \rho_w (1 - \psi), \quad (2.3)$$

$$\frac{\rho}{\mu} = \frac{\rho_a}{\mu_a} \psi + \frac{\rho_w}{\mu_w} (1 - \psi), \quad (2.4)$$

where  $\psi$  is the bubble volume fraction inside a numerical cell, and the subscripts  $a$  and  $w$  denote air and water, respectively. With this formulation, the continuity of tangential stresses at an interface is implicitly satisfied (Prosperetti 2002), and a smoother velocity profile is obtained around the interface in our preliminary rising single-bubble simulation than that with a volume-weighted arithmetic formulation ( $\rho = \rho_a \psi + \rho_w (1 - \psi)$  and  $\mu = \mu_a \psi + \mu_w (1 - \psi)$ ).

To track the phase interface, we use a level-set method (Herrmann 2008; Kim 2011):

$$\frac{\partial \phi}{\partial t} + \mathbf{u} \cdot \nabla \phi = 0, \quad (2.5)$$

where  $\phi$  is the level-set function which is a sign-distance function from the phase interface having positive and negative values in water and air, respectively. We use a refined level-set grid method (Herrmann 2008; Kim 2011), which adopts a separate refined level-set grid in addition to the flow solver grid, to reduce numerical errors coming from the volume and surface tension estimations. The bubble volume fraction  $\psi$  is calculated from the analytical formula of the level-set function (van der Pijl *et al.* 2005; Herrmann 2008). In this paper,  $r$ ,  $\theta$  and  $z$  denote the radial, azimuthal and axial directions, respectively, and  $x$  and  $y$  denote the horizontal directions in Cartesian coordinates. The numerical methods of solving (2.1), (2.2) and (2.5) are given in Appendix A.

We simulate both single-phase and monodispersed bubbly pipe flows. The fluids considered are air and water at atmospheric pressure and room temperature of 20 °C. The density and viscosity of air are  $\rho_a = 1.2 \text{ kg m}^{-3}$  and  $\mu_a = 1.8 \times 10^{-5} \text{ N s m}^{-2}$ , and those of water are  $\rho_w = 998 \text{ kg m}^{-3}$  and  $\mu_w = 1.0 \times 10^{-3} \text{ N s m}^{-2}$ , respectively (White 1979). The surface tension coefficient of the air–water interface is 0.07 N m and the gravitational acceleration is  $g = 9.81 \text{ m s}^{-2}$ . The water bulk Reynolds number is fixed at  $Re_{bulk} = \rho_w u_{bulk} D / \mu_w = 5300$ , where  $u_{bulk} (= \int (1 - \psi) u_z dV / \int (1 - \psi) dV = 0.132 \text{ m s}^{-1})$  is the water bulk velocity, and  $D (= 0.04 \text{ m})$  is the pipe diameter. These pipe diameter



and water bulk velocity are the same as those in the experiment by Lee *et al.* (2021). The corresponding friction Reynolds number of the single-phase pipe flow is  $Re_\tau = \rho_w u_\tau R / \mu_w = 180$  (Eggels *et al.* 1994), where  $u_\tau (= \sqrt{\tau_w / \rho_w})$  is the friction velocity,  $R$  is the pipe radius and  $\tau_w$  is the mean wall shear stress.

Figure 1 shows a schematic diagram of the present upward bubbly flow in a vertical pipe, grid indices for the momentum and level-set equations and grid distribution on a horizontal plane. As shown in figure 1(c), uniform grids are distributed on the whole domain, because small-scale flow structures are observed not only near the wall but also around the centre due to buoyant bubbles. The horizontal computational domain sizes for single-phase and bubbly flows are  $1.0079D$  ( $x$ )  $\times$   $1.0079D$  ( $y$ ) in Cartesian coordinates, and their axial domain sizes are  $7.5D$  and  $3D$ , respectively. The inclusion of  $0.0079D$  in the horizontal domain is due to the use of an immersed boundary method. We use a smaller axial domain size of  $3D$  for the present bubbly flow because the flow structures are smaller due to bubble–water interactions. We show below that this axial domain size is still large enough to capture flow structures in the bubbly flow. The number of grid points for the single-phase flow is  $256$  ( $x$ )  $\times$   $256$  ( $y$ )  $\times$   $384$  ( $z$ ). From our grid resolution test (see § 2.2), we suggest that the numbers of grid points per bubble required for the momentum and level-set equations are 24 and 48, respectively. Based on this requirement, for case SM, we provide  $384 \times 384 \times 1146$  and  $768 \times 768 \times 2292$  grid points for the momentum and level-set equations, respectively, whereas  $256 \times 256 \times 762$  and  $512 \times 512 \times 1524$  grid points are provided for other cases. The grid spacings in wall units are  $\Delta x^+ (= \Delta x u_\tau / \nu_w) = \Delta y^+ = 1.42$  and  $\Delta z^+ = 7.03$  for the single-phase flow, and  $\Delta x^+ = \Delta y^+ = \Delta z^+ = 1.7$ – $2.5$  for the bubbly flows. The periodic boundary condition is applied to the axial and horizontal directions, and the no-slip boundary condition is satisfied on the pipe wall (immersed boundary).

Table 1 shows the cases considered in this study, where the variations of the bubble equivalent diameter  $d_{eq} (= (6V_b/\pi)^{1/3}$ ;  $V_b$  is the volume of each bubble), total bubble volume fraction  $\langle \psi \rangle$ , number of bubbles  $N_{bub}$ , Eötvös number  $Eu (= \rho_w g d_{eq}^2 / \sigma)$ , friction Reynolds number  $Re_\tau$ , bubble Reynolds number  $Re_{bub} (= \rho_w (\langle u_{bub} \rangle - u_{bulk}) d_{eq} / \mu_w)$  and averaging time for obtaining statistics  $T_{avg}$  are listed for each case. Here,  $\langle u_{bub} \rangle$  is the overall mean bubble velocity averaged over all the bubbles in the computational domain. The bubble equivalent diameters considered are  $d_{eq} = 2.62, 3.30$  and  $4.16$  mm ( $d_{eq}/D = 0.0655, 0.0825$  and  $0.1040$ , respectively), and the corresponding Eötvös numbers are  $Eu = 0.96, 1.52$  and  $2.42$ , respectively. We also performed simulations at higher  $d_{eq}$  values ( $d_{eq}/D = 0.1310$  and  $0.1650$ ), but do not include their results here, because monodispersed bubbly flow could not be achieved due to breakup induced by turbulence.

Figure 2 shows the temporal variations of  $-\Pi$  to drive a constant water mass flow rate (or a constant water bulk Reynolds number) for all cases. Since the weight of the air–water mixture is constant in time, the behaviour of  $-\Pi$  essentially represents that of the mean pressure gradient. As the equivalent bubble diameter decreases at a given  $\langle \psi \rangle$  and total bubble volume fraction increases at a given  $d_{eq}$ , the mean pressure gradient (and  $Re_\tau$  in table 1) increases. The mean pressure gradients of bubbly flows exhibit large fluctuations as compared with that of the single-phase flow. These large fluctuations come from intermittent bubble–wall interactions, which is discussed in detail in § 3.2.

## 2.2. Validation

The use of an immersed boundary method for the present single-phase pipe flow is validated by comparing the turbulence statistics with those of Eggels *et al.* (1994) and

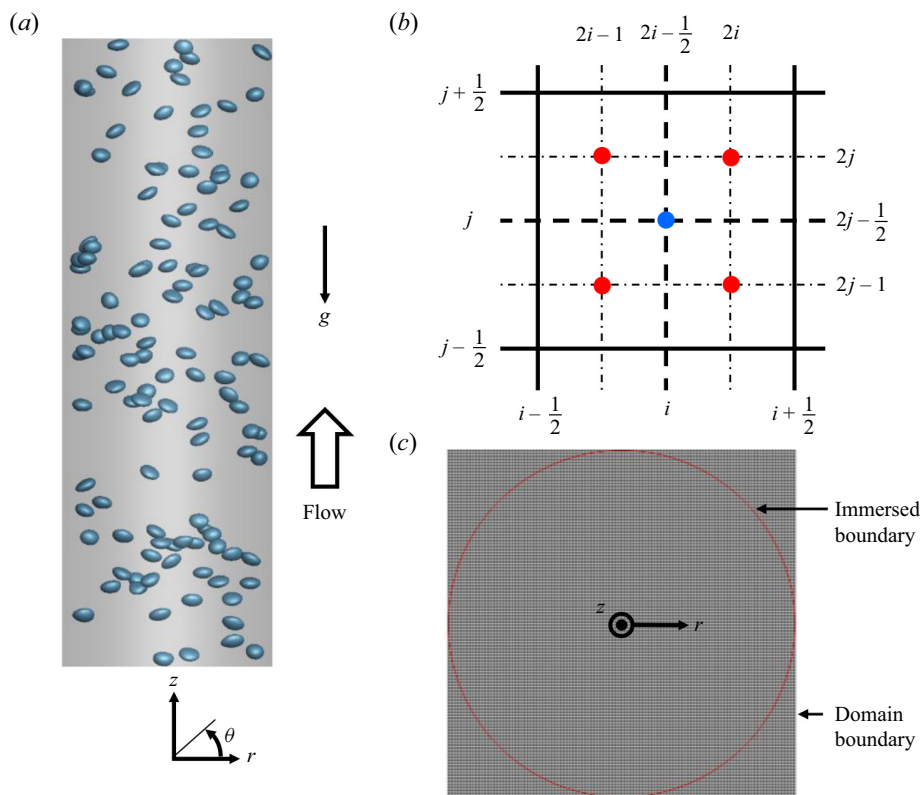


Figure 1. Numerical set-up: (a) schematic diagram of an upward bubbly flow in a vertical pipe; (b) grid systems for the momentum and level-set equations; (c) grids on a horizontal plane, computational boundary and immersed boundary (pipe wall). In (b), indices  $i$  and  $j$  are for the momentum equations, and indices  $2i$  and  $2j$  are for the level-set equation. Filled circles in blue and red are the numerical cell centres for the momentum and level-set equations, respectively.

Case	$d_{eq}/D$	$\langle\psi\rangle$ (%)	$N_{bub}$	$Eo$	$Re_{\tau}$	$Re_{bub}$	$T_{avg}u_{bulk}/D$
small-medium (SM)	0.0655	1.5	240	0.96	323	533	45
medium-medium (MM)	0.0825	1.5	120	1.52	285	737	59
large-medium (LM)	0.1040	1.5	60	2.42	256	1000	73
medium-low (ML)	0.0825	0.75	60	1.52	264	740	57
medium-high (MH)	0.0825	3.0	240	1.52	322	724	35

Table 1. Cases studied: bubble equivalent diameter, total bubble volume fraction, number of bubbles, Eötvös number, friction Reynolds number, bubble Reynolds number and averaging time for obtaining statistics. Here, the names of cases denote (relative size of  $d_{eq}$ )–(relative magnitude of  $\langle\psi\rangle$ ), respectively. That is, (small, medium, large) correspond to the cases of  $d_{eq} = (2.62, 3.30, 4.16 \text{ mm})$ , respectively, and (low, medium, high) represent the cases of  $\langle\psi\rangle = (0.75\%, 1.5\%, 3.0\%)$ , respectively. Note that small–medium–large and low–medium–high are used in terms of relative bubble size and volume fraction among the cases considered, and are not from absolute criteria for the bubble size and volume fraction.

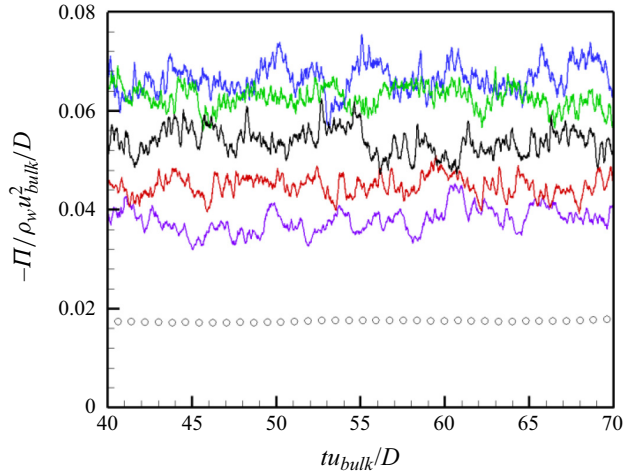


Figure 2. Temporal variations of  $-\Pi$  in (2.2): red, ML; black, MM; blue, MH; green, SM; violet, LM;  $\circ$ , single phase.

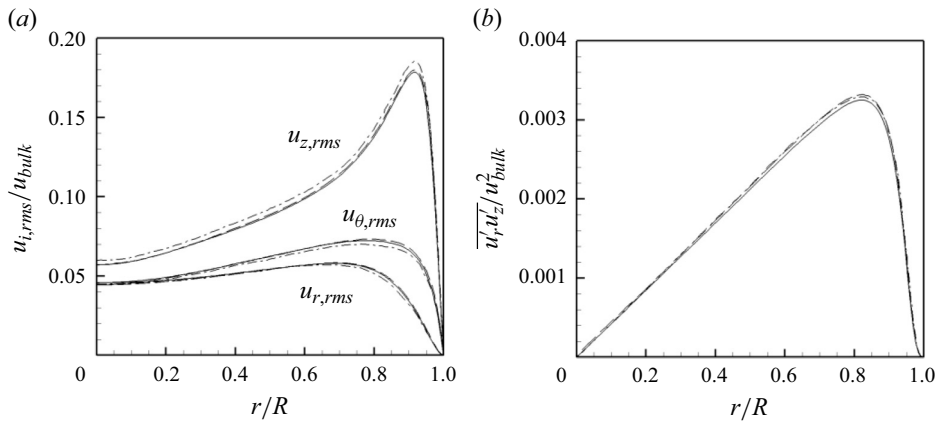


Figure 3. Profiles of the (a) r.m.s. velocity fluctuations and (b) Reynolds shear stress: —, present; ---, Eggels *et al.* (1994); — —, Wu & Moin (2009).

Wu & Moin (2009) at  $Re_{bulk} = 5300$ . The present grid spacings in Cartesian coordinates are uniform in all directions:  $\Delta x^+ = \Delta y^+ = 1.42$  and  $\Delta z^+ = 7.03$ . These magnitudes are in between those used in Eggels *et al.* (1994) ( $\Delta r^+ = 1.88$ ,  $R^+ \Delta \theta^+ = 8.84$ ,  $\Delta z^+ = 7.03$ ) and in Wu & Moin (2009) ( $\Delta r^+ = 0.167$ ,  $R^+ \Delta \theta^+ = 2.22$ ,  $\Delta z^+ = 5.31$ ) at the wall ( $r = R$ ). The present friction velocity obtained is  $u_\tau = 0.06779 u_{bulk}$ , and is very similar to  $0.06789 u_{bulk}$  (Eggels *et al.* 1994) and  $0.06844 u_{bulk}$  (Wu & Moin 2009). Figure 3 shows the Reynolds normal and shear stresses, together with those from Eggels *et al.* (1994) and Wu & Moin (2009). The present results agree very well with those of previous studies.

To examine if the axial domain size of  $L_z = 3D$  is appropriate for the present bubbly flow, the two-point correlation coefficients of the velocity fluctuations in the axial direction are calculated and shown in figure 4 for the case of ML (lowest bubble volume fraction). As shown,  $R_{ii}$ 's rapidly decrease with increasing  $r_z$  and approach nearly zero at  $r_z/D = 1.5$ , indicating that the current axial domain size of  $3D$  is reasonably large. Note that, in

single-phase pipe flow, low-speed streaks near the wall extend up to 1000 viscous wall units (Eggels *et al.* 1994), and thus the axial domain size should be larger than about  $6D$  ( $D^+ = 360$ ) to contain at least two streaky structures. As we discuss later, in bubbly flow, the near-wall streaky structures are rarely found in the present bubbly flow due to the agitation by bubbles. We also increase the axial domain size to  $L_z = 6D$  for case ML, and provide results in figure 5 together with those for  $L_z = 3D$ . As shown, the mean bubble volume fraction  $\bar{\psi}$  and the r.m.s. velocity fluctuations from two different axial domain sizes show negligible changes, indicating that  $L_z = 3D$  is sufficiently large. On the other hand, it was shown by Risso & Ellingsen (2002) that for a single rising air bubble of a diameter comparable to the present one in stagnant water, the wake behind the bubble persists over dozens of bubble diameters. Thus, a small axial domain size may change the wake characteristics of the bubble. To see if this happens for the present simulation, we calculate the differences between the time-averaged and ensemble-averaged water flow variables (axial velocity and turbulent kinetic energy) for case ML. Here, the time-averaged axial velocity and turbulent kinetic energy ( $\bar{u}_z$  and  $\frac{1}{2}\overline{u'_i u'_i}$ , respectively) are obtained using the process in (3.1) below, and the ensemble-averaged axial velocity and turbulent kinetic energy ( $\tilde{u}_z$  and  $\frac{1}{2}\widetilde{u''_i u''_i}$  ( $u''_i = u_i - \tilde{u}_i$ ), respectively) are obtained by averaging the instantaneous water velocity fields around bubbles located at  $|r - r_o| \leq 0.5\Delta r$  ( $\Delta r = 0.0039D$ ) for two different radial positions  $r_o/R = 0.5$  and  $0.89$ . The results as a function of the axial distance from the bubble centre ( $z_o$ ) are shown in figure 6. As shown, both  $\tilde{u}_z - \bar{u}_z$  and  $\frac{1}{2}(\widetilde{u''_i u''_i} - \overline{u'_i u'_i})$  are positive near the wake because the bubble velocity is greater than the water velocity, and are nearly zero at  $(z - z_o)/d_{eq} \approx -2.5$  ( $(z - z_o)/D \approx -0.21$ ), indicating that the bubble wake quickly disappears in turbulent bubbly flow unlike that from a single rising bubble. Therefore, the use of  $L_z = 3D$  does not influence the bubble dynamics in turbulent bubbly flow.

For the validation of the present numerical method, we conduct simulations of a rising air bubble with a straight path in water–glycerol mixtures considered by Raymond & Rosant (2000), where  $d_{eq} = 3, 5$  and  $7$  mm,  $\sigma_{sol}/\sigma_w = 0.91$ ,  $\rho_{sol}/\rho_w = 1.20, 1.19, 1.17$  and  $1.15$  and  $\mu_{sol}/\mu_w = 73.3, 42.2, 24.0$  and  $13.0$  for solutions with  $\psi_w$  (water volume fraction) = 18 %, 24 %, 31 % and 40 %, respectively, and the subscript ‘sol’ denotes the solution. The computational domain size is  $(L_x, L_y, L_z) = (4d_{eq}, 4d_{eq}, 20d_{eq})$ , and the numbers of grid points per bubble equivalent diameter are  $n_{NS} = 16$  and  $n_{LS} = 32$  for the momentum and level-set equations, respectively. Table 2 shows the variation of the terminal velocity of air bubbles with the water volume fraction, together with the experimental results by Raymond & Rosant (2000). As shown in this table, the present results are in excellent agreement with the experimental ones.

We also conduct simulations of a rising air bubble in stagnant water to examine how many grid points should be located per bubble such that bubble dynamics is correctly represented. We choose the largest bubble ( $d_{eq} = 4.16$  mm) among those considered in the present study for these simulations. The grid resolutions tested for the Navier–Stokes and level-set equations are  $(d_{eq}/\Delta x_{NS}, d_{eq}/\Delta x_{LS}) = (8, 16), (16, 32), (24, 48)$  and  $(32, 64)$ , respectively. This bubble requires a vertical computational domain size of  $100d_{eq}$  to obtain a bubble path in equilibrium, which requires too much computational cost. Therefore, we rather use a periodic computational box in all directions with a size of  $(L_x, L_y, L_z) = (4d_{eq}, 4d_{eq}, 20d_{eq})$ . With this numerical set-up, the wake behind a bubble affects its trajectory, and thus the bubble trajectory should be different from that obtained in a very large domain size. However, this numerical set-up is sufficient to examine the resolution requirement at a much lower computational cost. Figure 7 shows the trajectories of the rising bubble for different grid resolutions. The bubble trajectory from

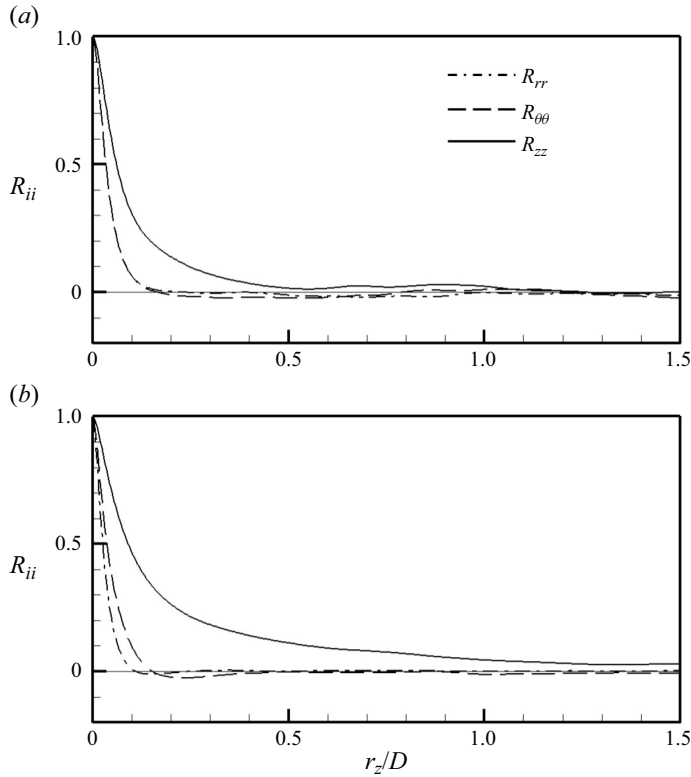


Figure 4. Two-point correlation coefficients of the velocity fluctuations  $R_{ii}$  as a function of the axial separation distance  $r_z$  (case ML): (a)  $r/R = 0.20$ ; (b)  $r/R = 0.95$ .

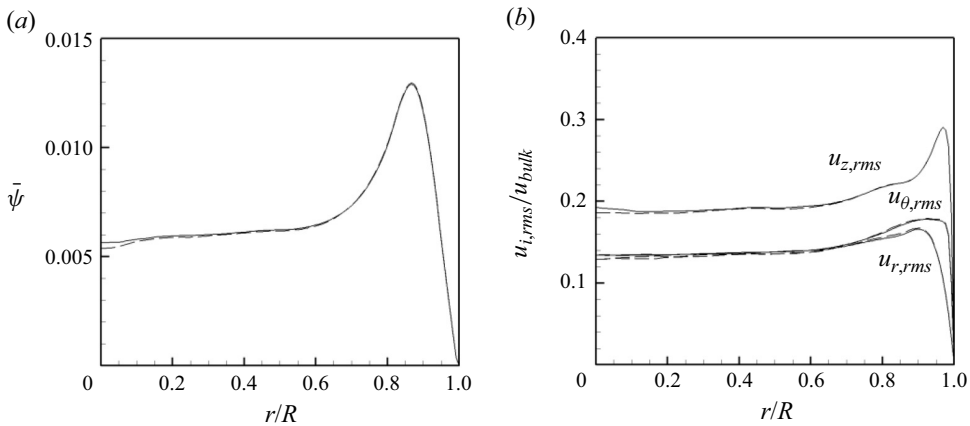


Figure 5. Profiles of the (a) mean bubble volume fraction and (b) r.m.s. velocity fluctuations for different axial domain sizes (case ML): —,  $L_z = 3D$ ; ---,  $L_z = 6D$ .

$(d_{eq}/\Delta x_{NS}, d_{eq}/\Delta x_{LS}) = (8, 16)$  is rectilinear, while others are oscillatory. The onsets of oscillatory trajectories occur at the same vertical position ( $z/d_{eq} = 5.5$ ) when the initial bubble location is  $z/d_{eq} = 2$ , but the subsequent trajectories are different for different grid resolutions. Due to the use of Cartesian coordinates and the relative position of

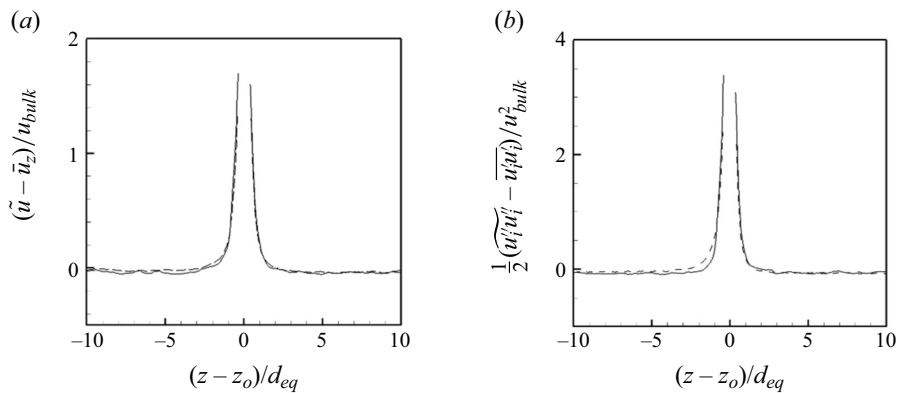


Figure 6. Axial profiles of the differences in the time-averaged and ensemble-averaged water flow variables near a bubble (case ML): (a)  $\tilde{u}_z - \bar{u}_z$  (axial velocity); (b)  $(\tilde{u}_i^2 u_i^2 - \bar{u}_i^2 u_i^2)/2$  (turbulent kinetic energy); —,  $r_o/R = 0.5$ ; - - -,  $r_o/R = 0.89$ .

$\psi_w$ (%)	$d_{eq}$ (mm)	$Eo$	$u_T$ (m s <sup>-1</sup> ) (present)	$u_T$ (m s <sup>-1</sup> ) (Raymond & Rosant 2000)	Error (%)
18	3	1.66	0.0827	0.0937	-11.74
	5	4.62	0.1557	0.1668	-6.65
	7	9.05	0.1952	0.2065	-5.47
24	3	1.64	0.1175	0.1268	-7.33
	5	4.56	0.1914	0.2056	-6.91
	7	8.93	0.2227	0.2276	-2.15
31	3	1.64	0.1575	0.1563	0.77
	5	4.56	0.2257	0.2331	-3.17
40	3	1.64	0.2039	0.1985	2.72

Table 2. Variation of the terminal velocity  $u_T$  with the water volume fraction  $\psi_w$  (single rising air bubble in water-glycerol solution). The experimental data of Raymond & Rosant (2000) are also shown for comparison.

the bubble to the grid, the same trajectory is not expected even with a larger number of grid points. Although the trajectories are different for different grid resolutions, their characteristics from  $(d_{eq}/\Delta x_{NS}, d_{eq}/\Delta x_{LS}) = (24, 48)$  and  $(32, 64)$  are very similar to each other. For example, their dominant frequencies of oscillation,  $f_{path}\sqrt{d_{eq}/g}$ , obtained from the power spectra of the bubble locations on the projected horizontal plane  $(x, y)$  are 0.111 and 0.115, respectively, while that from  $(d_{eq}/\Delta x_{NS}, d_{eq}/\Delta x_{LS}) = (16, 32)$  is 0.056. This result suggests that the resolution of  $(24, 48)$  should adequately predict the bubble behaviour in water. Figure 8 shows the temporal variations of vertical and horizontal velocities of the rising bubble for different grid resolutions. As shown,  $(d_{eq}/\Delta x_{NS}, d_{eq}/\Delta x_{LS}) = (8, 16)$  provides very different velocities from those from denser resolutions. The results from the grid resolutions of  $(24, 48)$  and  $(32, 64)$  are very similar to each other, and those of  $(16, 32)$  are slightly different in terms of oscillation frequency and amplitude from those of  $(24, 48)$  and  $(32, 64)$ . The time-averaged terminal velocities from  $(d_{eq}/\Delta x_{NS}, d_{eq}/\Delta x_{LS}) = (8, 16)$ ,  $(16, 32)$ ,  $(24, 48)$  and  $(32, 64)$  are  $1.05$ ,  $1.19$ ,  $1.21$  and  $1.20\sqrt{gd_{eq}}$ , respectively. Therefore, for the bubble of  $d_{eq} = 4.16$  mm, grid points of  $(24, 48)$  per bubble for the Navier–Stokes and level-set equations, respectively, are required for describing bubble dynamics, and grid points of  $(16, 32)$  are quite marginal.



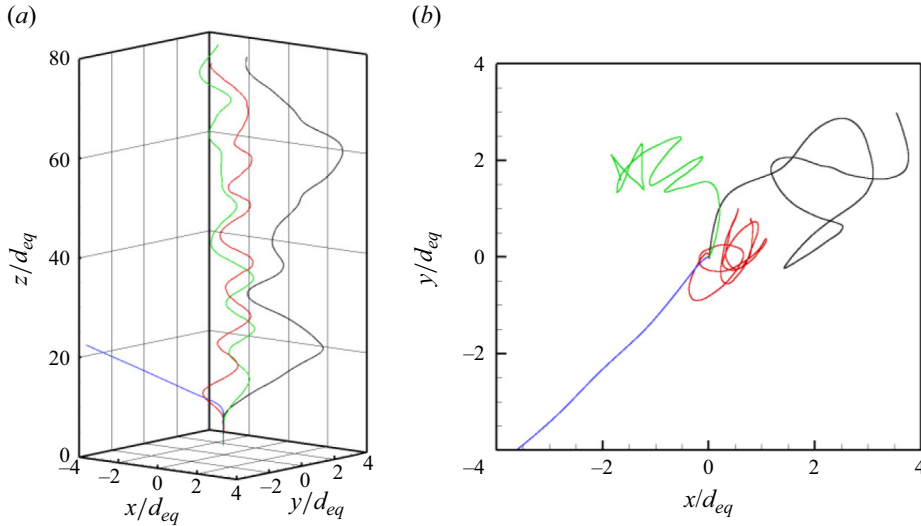


Figure 7. Trajectories for a rising bubble ( $d_{eq} = 4.16$  mm) in the periodic domain with varying grid spacing: (a) three-dimensional view; (b) top view. Blue,  $(d_{eq}/\Delta x_{NS}, d_{eq}/\Delta x_{LS}) = (8, 16)$ ; black,  $(16, 32)$ ; green,  $(24, 48)$ ; red,  $(32, 64)$ .

For a smaller size of bubble, the corresponding bubble Reynolds number becomes smaller and thus fewer grid points may be required. In our main simulations, we locate  $(d_{eq}/\Delta x_{NS}, d_{eq}/\Delta x_{LS}) = (25.2, 50.3)$ ,  $(21.1, 42.2)$  and  $(26.6, 53.2)$  for  $d_{eq} = 2.62, 3.30$  and  $4.16$  mm, respectively, according to this resolution study. Cano-Lozano *et al.* (2016) and Innocenti *et al.* (2021) used a volume of fluid (VoF) method to predict the dynamics of a single bubble and bubble swarm in still water at  $Re_{bub} = O(100)$ , respectively, and suggested by rigorously examining the bubble path, wake dynamics and bubble shape that a resolution of  $d_{eq}/\Delta x_{NS} \approx 100$  should be required. Zhang, Ni & Magnaudet (2021, 2022) also used the same method to predict the dynamics of a pair of bubbles rising in line at  $Re_{bub} = O(10)–O(100)$ , and indicated that  $d_{eq}/\Delta x_{NS} = 136$  is required in the vicinity of bubbles to resolve the boundary layer and wake. Unlike those studies, we examine the turbulence characteristics of bubbly pipe flow (multiple bubbles interacting with the wall) using a marginal number of grid points, and thus the present resolution may not be sufficient to accurately capture small-scale motions behind the bubbles. Such a rigorous analysis conducted by Cano-Lozano *et al.* (2016), Innocenti *et al.* (2021) and Zhang *et al.* (2021, 2022) could be a formidable task for the present flow.

### 3. Turbulence statistics and flow structures

#### 3.1. Turbulence statistics

Figure 9 shows the profiles of the mean bubble volume fraction in the radial direction for five bubbly flows. Note that cases ML, MM and MH have the same  $d_{eq}/D (= 0.0825)$  but different  $\langle \psi \rangle$  values of 0.75 %, 1.5 % and 3.0 %, respectively, and cases SM, MM and LM have the same  $\langle \psi \rangle (= 1.5 \%)$  but different  $d_{eq}/D$  values of 0.0655, 0.0825 and 0.1040, respectively. Except for case LM, the four other cases exhibit radial bubble distributions with peaks near the wall (called wall-peaking) and nearly flat profiles at the pipe centre region. Half the averaging time ( $T_{avg}$ ) in table 1 did not change the statistics near the

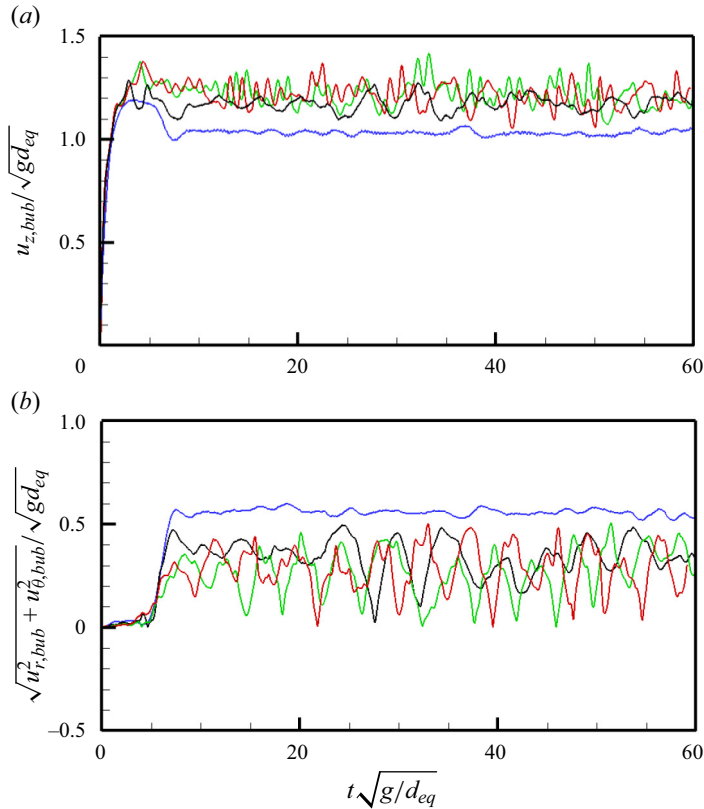


Figure 8. Temporal variations of the vertical and horizontal velocities for a rising bubble ( $d_{eq} = 4.16$  mm) in the periodic domain with varying grid spacing: (a) vertical velocity; (b) horizontal velocity. Blue,  $(d_{eq}/\Delta x_{NS}, d_{eq}/\Delta x_{LS}) = (8, 16)$ ; black,  $(16, 32)$ ; green,  $(24, 48)$ ; red,  $(32, 64)$ .

wall but showed slight changes in the centre region (not shown here). Thus, further time averaging should provide slightly better profiles in the centre region, but requires significant amounts of additional computational time (the same argument is applied to the Reynolds normal stress profiles shown in figure 11). Case LM shows that the bubble distribution increases from the centre to  $r/R = 0.4$  and is nearly uniform at  $r/R = 0.4$ – $0.8$ , followed by a sharp decrease to the wall. This distribution lies between the wall-peaking and core-peaking bubble distributions. According to Dabiri *et al.* (2013), the direction of the lift force on a deformable bubble in wall-bounded upward bubbly flow depends on the magnitude of  $Eo$ : i.e. bubbles move towards the centre for  $Eo > Eo_c$  ( $\approx 2.5$ ) and to the wall otherwise. As shown in table 1,  $Eo = 2.42$  (slightly smaller than  $Eo_c$ ) for case LM, whereas  $Eo$ 's are much smaller than  $Eo_c$  for the four other cases. Therefore, for case LM, more bubbles move away from the wall but do not reach the centre, whereas most bubbles move towards the wall for the four other cases. For a given  $\langle\psi\rangle$  (cases SM, MM and LM), more bubbles move to the wall with decreasing  $d_{eq}$ . On the other hand, for a given bubble equivalent diameter (i.e. same  $Eo$ ; cases ML, MM and MH),  $\bar{\psi}$  monotonically increases at all  $r$ 's with increasing  $\langle\psi\rangle$ .

Figure 10 shows the profiles of the mean velocities of water and bubbles and relative mean bubble velocity in the radial direction for the single-phase and bubbly flows. Here,

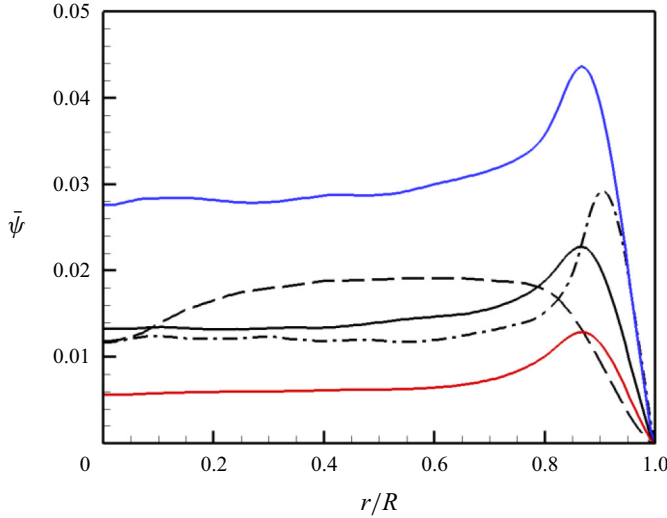


Figure 9. Profiles of the mean bubble volume fraction in the radial direction. Red curve, case ML ( $d_{eq}/D = 0.0825$  and  $\langle\psi\rangle = 0.75\%$ ); solid black curve, case MM ( $d_{eq}/D = 0.0825$  and  $\langle\psi\rangle = 1.5\%$ ); blue curve, case MH ( $d_{eq}/D = 0.0825$  and  $\langle\psi\rangle = 3.0\%$ ); dot-dashed curve, case SM ( $d_{eq}/D = 0.0655$  and  $\langle\psi\rangle = 1.5\%$ ); dashed curve, case LM ( $d_{eq}/D = 0.1040$  and  $\langle\psi\rangle = 1.5\%$ ).

the mean water and bubble velocities are obtained as

$$\bar{u}_z(r) = \frac{\int_0^T \int_0^{L_z} \int_0^{2\pi} (1 - \psi) u_z d\theta dz dt}{\int_0^T \int_0^{L_z} \int_0^{2\pi} (1 - \psi) d\theta dz dt}, \quad (3.1)$$

$$\bar{u}_{z,bub}(r) = \frac{1}{T} \int_0^T \left\{ \frac{1}{N_{bub}(r, t)} \sum_{i=1}^{N_{bub}(r, t)} \frac{1}{V_{b_i}} \int_{V_{b_i}} u_z dV \right\} dt, \quad (3.2)$$

where  $T$  is the integration time,  $L_z$  is the axial domain size,  $N_{bub}(r, t)$  is the number of bubbles whose centres of mass are located at  $r - 0.00625D \leq r_{cm} < r + 0.00625D$  at time  $t$  and  $V_{b_i}$  is the volume of corresponding bubble  $i$ . The water flows with bubbles have higher mean shear rates near the wall than the single-phase flow because of the buoyant bubbles located close to the wall. As the bubble concentration near the wall increases with increasing  $\langle\psi\rangle$  (ML to MH) and decreasing  $d_{eq}$  (LM to SM) (see figure 9), the mean shear rates near and at the wall increase (see also  $Re_\tau$ 's in table 1). On the other hand, the mean water velocities of bubbly flows near the centre are lower than that of the single-phase flow and decrease with increasing  $\langle\psi\rangle$  and decreasing  $d_{eq}$  owing to the constant mass flow rate. The magnitudes of the mean bubble velocities are greater than two times those of the mean water velocities, and those near the centre increase with decreasing  $\langle\psi\rangle$  and increasing  $d_{eq}$  (a similar observation was made in homogeneous bubbly flows by Riboux *et al.* (2010) and Roghair *et al.* (2011)). Hence, the relative mean bubble velocities are always positive for the present flows because  $\bar{u}_{z,bub} > \bar{u}_z$ . At  $r/R < 0.8$ , the relative mean bubble velocity is almost constant (indicating negligible wall effect in this radial region), and increases slightly with decreasing  $\langle\psi\rangle$ . However, at  $r/R > 0.8$ , the relative mean bubble velocity rapidly decreases because the mean bubble velocity rapidly decreases towards the

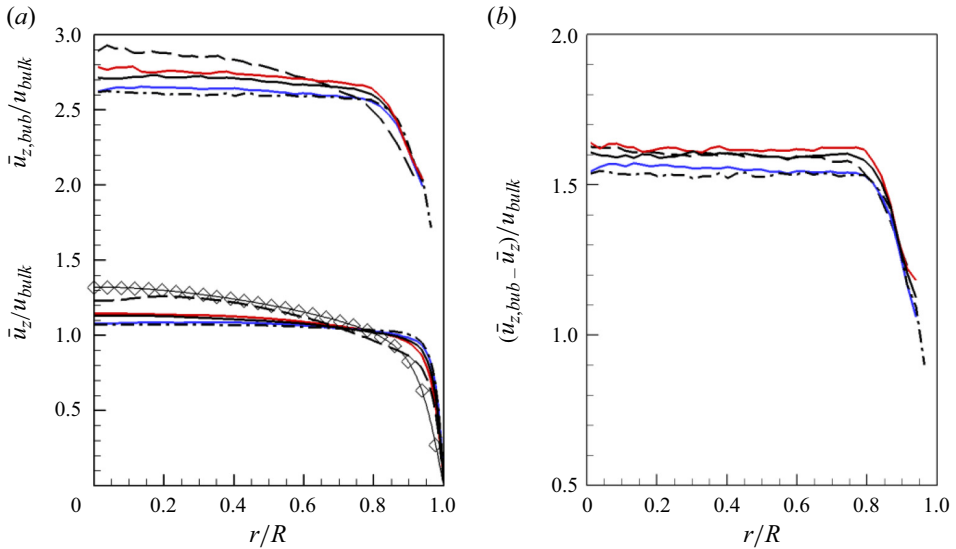


Figure 10. Profiles of the mean water and bubble velocities, and relative mean bubble velocity in the radial direction: (a) mean velocities (water and bubble); (b) relative mean bubble velocity.  $\diamond$ , Single phase; red, case ML; solid black, MM; blue, MH; dot-dashed, SM; dashed, LM.

wall while the mean water velocity there increases due to rising bubbles compared with single-phase flow.

Figure 11(a–c) shows the profiles of the r.m.s. water velocity fluctuations in the radial direction for the single-phase and bubbly flows. The bubbly flows have much higher r.m.s. velocity fluctuations at all radial locations than those of the single-phase flow. The r.m.s. velocity fluctuations increase with increasing  $\langle\psi\rangle$  and  $d_{eq}$ . The behaviours of the r.m.s. velocity fluctuations near the centre are similar to those of the mean bubble volume fraction at each radial position (see figure 9): i.e. the magnitudes increase from  $r/R = 0$  to 0.4 for case LM but are nearly uniform for the other four cases. This is because the fluctuations induced by bubbles are closely related to the number of bubbles present. The axial r.m.s. velocity fluctuations near the wall also show similar behaviours to those of  $\bar{\psi}$ , but their peak locations are at  $r/R \approx 0.97$ , while the peak of  $\bar{\psi}$  locates at  $r/R = 0.85$ – $0.9$ . This phenomenon (i.e. shift of the peak locations) is discussed in detail in § 3.2. The radial and azimuthal r.m.s. velocity fluctuations gradually increase towards the wall as compared to the axial velocity component, because these cross-flow components are affected by the wake behind rising bubbles but the axial component is directly influenced by them. Since  $\bar{\psi}$  monotonically increases at all the radial locations with increasing  $\langle\psi\rangle$  (figure 9), the increases of the r.m.s. velocity fluctuation with  $\langle\psi\rangle$  can be normalized by introducing  $\bar{\psi}$ . Figure 11(d) shows the r.m.s. water velocity fluctuations normalized by  $u_{bulk}$  and  $\bar{\psi}^{0.4}$  for cases ML, MM and MH ( $\bar{\psi} = 0.75, 1.5$  and  $3.0$ , respectively, with the same  $d_{eq}/D = 0.0825$ ). Here,  $\bar{\psi}^{0.4}$  comes from the studies of homogeneous bubbly flows (Risso & Ellingsen 2002; Martínez-Mercado, Palacios-Morales & Zenit 2007; Roig & De Tournemine 2007; Riboux *et al.* 2010) and laminar bubbly pipe flow (Kim, Lee & Park 2016). With this normalization, the profiles of r.m.s. velocity fluctuations for three cases collapse well among themselves at all the radial locations.

As mentioned in § 1, turbulent bubbly flows contain both shear-induced and bubble-induced turbulence. If the shear-induced and bubble-induced turbulence are

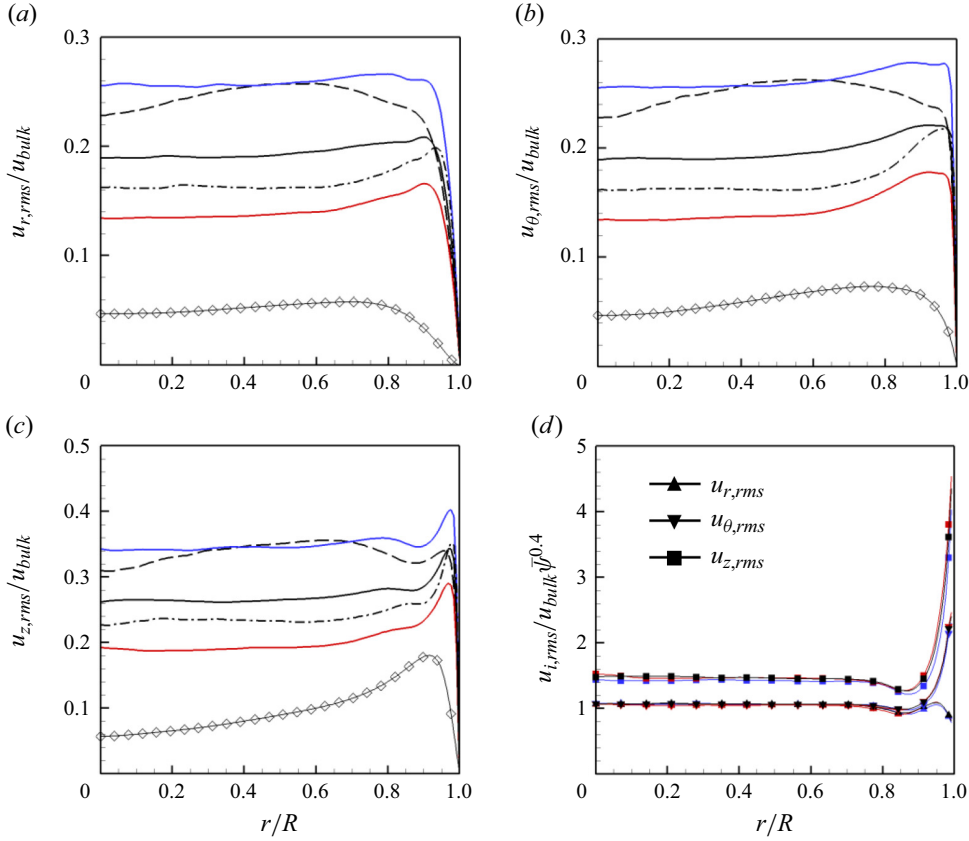


Figure 11. Profiles of the r.m.s. water velocity fluctuations in the radial direction: (a)  $u_{r,rms}$ ; (b)  $u_{\theta,rms}$ ; (c)  $u_{z,rms}$ ; (d)  $u_{i,rms}/(u_{bulk}\bar{\psi}^{0.4})$ .  $\diamond$ , Single phase; red, case ML; solid black, MM; blue, MH; dot-dashed, SM; dashed, LM. In (d), only the cases ML, MM and MH are shown.

assumed to be independent from each other, one may decompose the Reynolds normal stresses  $\overline{u'_\alpha u'_\alpha}$  as

$$\overline{u'_\alpha u'_\alpha} = R_{SIT} + R_{BIT}, \quad (3.3)$$

where  $R_{SIT}$  and  $R_{BIT}$  denote the Reynolds normal stresses from the shear-induced and bubble-induced turbulence, respectively. Since  $R_{BIT} \sim \bar{\psi}^{0.8}$  (Risso & Ellingsen 2002; Martínez-Mercado *et al.* 2007; Roig & De Tournemine 2007; Riboux *et al.* 2010; Kim *et al.* 2016), the results in figure 11(d) indicate that the bubble-induced turbulence is predominant even near the wall for the present flows. Note that Lu & Tryggvason (2008), Dabiri *et al.* (2013) and Du Cluzeau *et al.* (2019) indicated the existence of an interaction between the shear-induced and bubble-induced turbulence from their wall-bounded upward bubbly flows. Since their density ratios ( $\rho_{bubble}/\rho_{liquid}$ ) considered were about 100 times larger than that of the present study, their bubble-induced turbulence was much weaker than the present one, leading to different conclusions on the effect of the bubble-induced turbulence. The instantaneous flow structures regarding bubble-induced turbulence are discussed later in this paper. In Appendix B, we suggest a modified algebraic RANS model considering the interaction between shear-induced and bubble-induced turbulence for better predictions of the mean axial velocity and wall

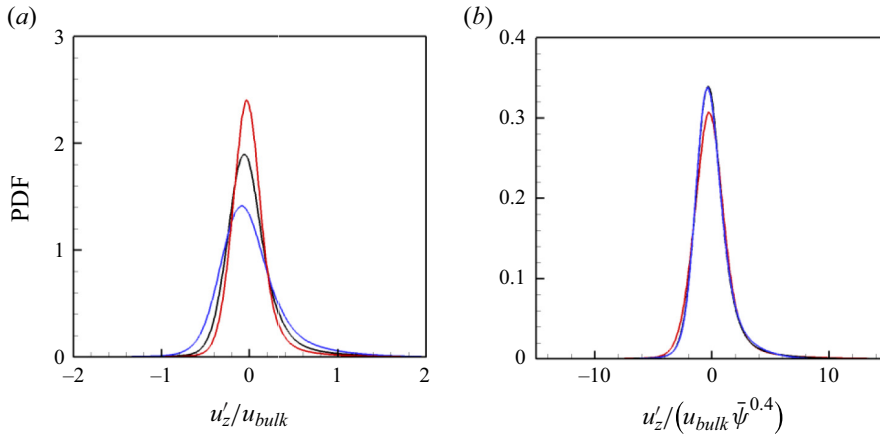


Figure 12. PDFs of the axial water velocity fluctuations at  $r/R = 0.88$  normalized by (a)  $u_{bulk}$  and (b)  $u_{bulk}\bar{\psi}^{0.4}$ ; red, case ML; black, MM; blue, MH.

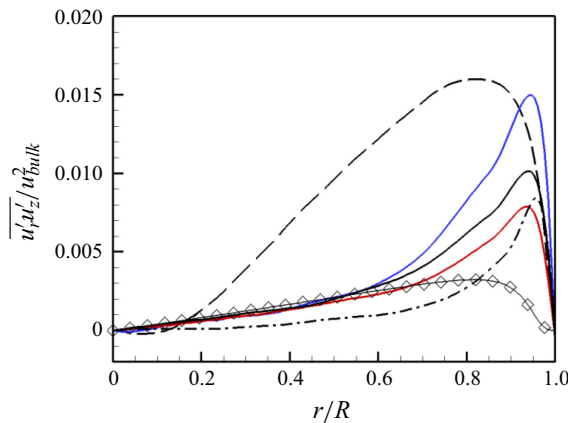


Figure 13. Profiles of the water Reynolds shear stress in the radial direction:  $\diamond$ , single phase; red, case ML; solid black, MM; blue, MH; dot-dashed, SM; dashed, LM.

shear stress for a wider range of liquid bulk Reynolds numbers than those of the previous algebraic RANS model (Sato *et al.* 1981a).

Figure 12 show the probability density functions (PDFs) of the axial velocity fluctuations with normalizations with and without  $\bar{\psi}^{0.4}$  at  $r/R = 0.88$  for three different  $\langle\psi\rangle$ . As  $\langle\psi\rangle$  increases, the peak of PDF normalized by  $u_{bulk}$  decreases and the PDF becomes widened. On the other hand, when normalized by  $u_{bulk}\bar{\psi}^{0.4}$ , the three PDFs collapse quite well as observed from homogeneous bubbly flows (Risso & Ellingsen 2002; Riboux *et al.* 2010), again indicating that the bubble-induced turbulence is dominant for the present bubbly flows. Similar results are observed for the azimuthal and radial velocities and at other radial locations.

Figure 13 shows the profiles of the water Reynolds shear stress in the radial direction for the single-phase and bubbly flows. The Reynolds shear stress near the wall is much larger due to bubbles than that of the single-phase flow. With increasing  $d_{eq}$  (cases SM, MM and LM), the Reynolds shear stress increases over all the radial locations except very near



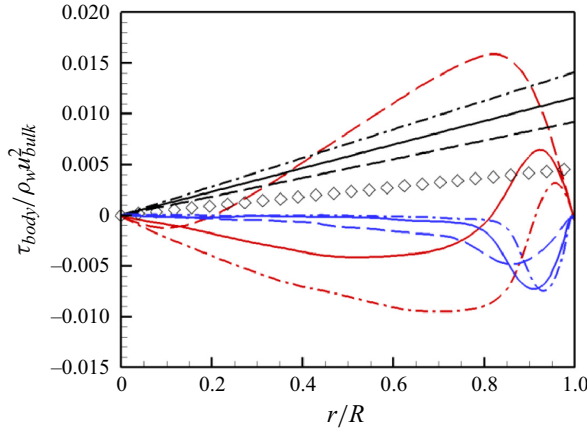


Figure 14. Profiles of the body forces in the radial direction: black lines,  $\tau_\beta$ ; red lines,  $\tau_{grav}$ ; blue lines,  $\tau_{surf}$ .  $\diamond$ , Single phase ( $\tau_\beta$  only); dot-dashed, case SM; solid, MM; dashed, LM.

the centre where  $\overline{u'_r u'_z}$  is close to zero. On the other hand, with increasing  $\langle \psi \rangle$  (cases ML, MM and MH), it increases more near the wall but does not change at the centre region ( $r < 0.5R$ ). Hence, normalization with  $\bar{\psi}^{0.8}$  works only for the Reynolds normal stresses, not for the Reynolds shear stress, again indicating that the effect of the shear-induced turbulence is very weak for the present flows.

Figure 14 shows the profiles of the body forces in the radial direction for cases SM, MM and LM, together with those of the single-phase flow. The axial RANS equation integrated over the radial direction is

$$\overline{\rho u'_r u'_z} - \mu \frac{\partial \overline{u_z}}{\partial r} = -\frac{r}{2} \Pi - \frac{1}{r} \int_0^r (\bar{\rho} - \langle \rho \rangle) g r \, dr + \frac{1}{r} \int_0^r \sigma \kappa n_z \delta r \, dr, \quad (3.4)$$

where the first and second terms on the left-hand side are the Reynolds and viscous shear stresses, respectively, and the first, second and third terms on the right-hand side are the mean pressure gradient ( $\tau_\beta$ ), gravitational force ( $\tau_{grav}$ ) and surface tension ( $\tau_{surf}$ ) terms, respectively. For the single-phase flow, the sum of the Reynolds and viscous shear stresses is proportional to  $r$ . However, for the bubbly flows, it is not linear because of additional gravitational force and surface tension terms that have peaks near the wall. The gravitational force term, which is closely related to the mean bubble volume fraction in that  $\bar{\rho} - \langle \rho \rangle = -(\rho_w - \rho_a)(\bar{\psi} - \langle \psi \rangle)$ , significantly changes depending on the bubble equivalent diameter  $d_{eq}$ , while the surface tension term changes relatively little. For case LM, the Reynolds shear stress is much larger at the entire region except near the centre than that of the single-phase flow (figure 13). This is because the gravitational force term is highly positive in the entire region except near the centre and is much larger than the negative surface tension term. As the bubble size gets smaller (from case LM to cases MM and SM), the bubble distribution changes from flat to wall-peaking (see figure 9). Then, the region with  $\bar{\rho}(r) > \langle \rho \rangle$  spreads from the centre to the wall, and thus the region with negative  $\tau_{grav}$  becomes wider. On the other hand,  $\tau_{surf}$  is negative, especially near the wall (see figure 16(f) for explanation), and does not much change with  $d_{eq}$ . Furthermore, its magnitude near the wall is comparable to that of the mean pressure gradient. Tanaka (2011) and Du Cluzeau *et al.* (2019) also numerically observed negative surface tension near the wall, but the underlying reason was not extensively studied. This surface tension term was not taken into account when the profile of  $\overline{u'_r u'_z}$  was obtained using (3.4) in experimental

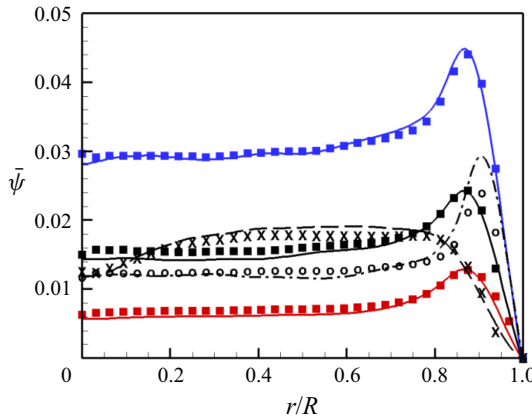


Figure 15. Comparison of  $\bar{\psi}$ 's (symbols) predicted from (3.5) with those (lines) directly from the present numerical simulations: red and squares, case ML; solid black and squares, case MM; blue and squares, case MH; dot-dashed and circles, case SM; dashed and crosses, case LM.

studies (Wang 1986; Colin *et al.* 2012), as it was challenging to experimentally measure the surface tension. Thus, the Reynolds shear stress profile obtained in those studies matched well the experimental data except near the wall.

Equation (3.4) can be used to calculate the mean bubble volume fraction by multiplying this equation by  $r$ , differentiating the resulting equation with respect to  $r$  and introducing  $\bar{\rho} - \langle \rho \rangle = -(\rho_w - \rho_a)(\bar{\psi} - \langle \psi \rangle)$ :

$$\bar{\psi}(r) = \langle \psi \rangle + \frac{1}{(\rho_w - \rho_a)g} \left\{ \frac{1}{r} \frac{\partial}{\partial r} (r \overline{\rho u_r' u_z'}) - \frac{1}{r} \frac{\partial}{\partial r} \left( r \overline{\mu \frac{\partial u_z}{\partial r}} \right) + \Pi - \sigma \overline{\kappa n_z \delta} \right\}. \quad (3.5)$$

This equation can be also directly obtained from the time-averaged Navier–Stokes equation. Figure 15 shows a comparison of  $\bar{\psi}$ 's from (3.5) with that directly from the present numerical simulations for all the cases considered. As expected, two mean bubble volume fractions calculated as a function of the radial direction agree very well for all the cases.

### 3.2. Bubble behaviours and instantaneous vortical structures

Figure 16(a–c) shows the bubble trajectories for cases SM, MM and LM. Note that the number of trajectories in each panel is ten and these trajectories are taken at different time instants. Here, the mean major axis length of bubbles  $l_{bub}(r)$  is obtained by calculating the second moment of inertia of the bubbles whose centres of mass are located at  $r - 0.00625D \leq r_{cm} < r + 0.00625D$ , assuming an ellipsoidal shape, for the purpose of estimating the bubble–wall collision. As shown, when bubbles rise near the wall, they mainly bounce against the wall rather than slide along the wall or hang around the wall without collision. As  $deq$  decreases (from LM to SM), more bubbles frequently bounce against the wall. Figure 16(d,e) shows how the mean radial and axial bubble velocities change when bubbles move towards the wall and centre, respectively. Near the wall, the radial velocity for the bubbles moving towards the wall is much higher than that moving towards the centre, while the axial velocities for the bubbles moving to and away from the wall are quite similar to each other. Since a bubble moves in water, its shape is deformed into an ellipsoid such that the direction of the major axis is orthogonal to the bubble

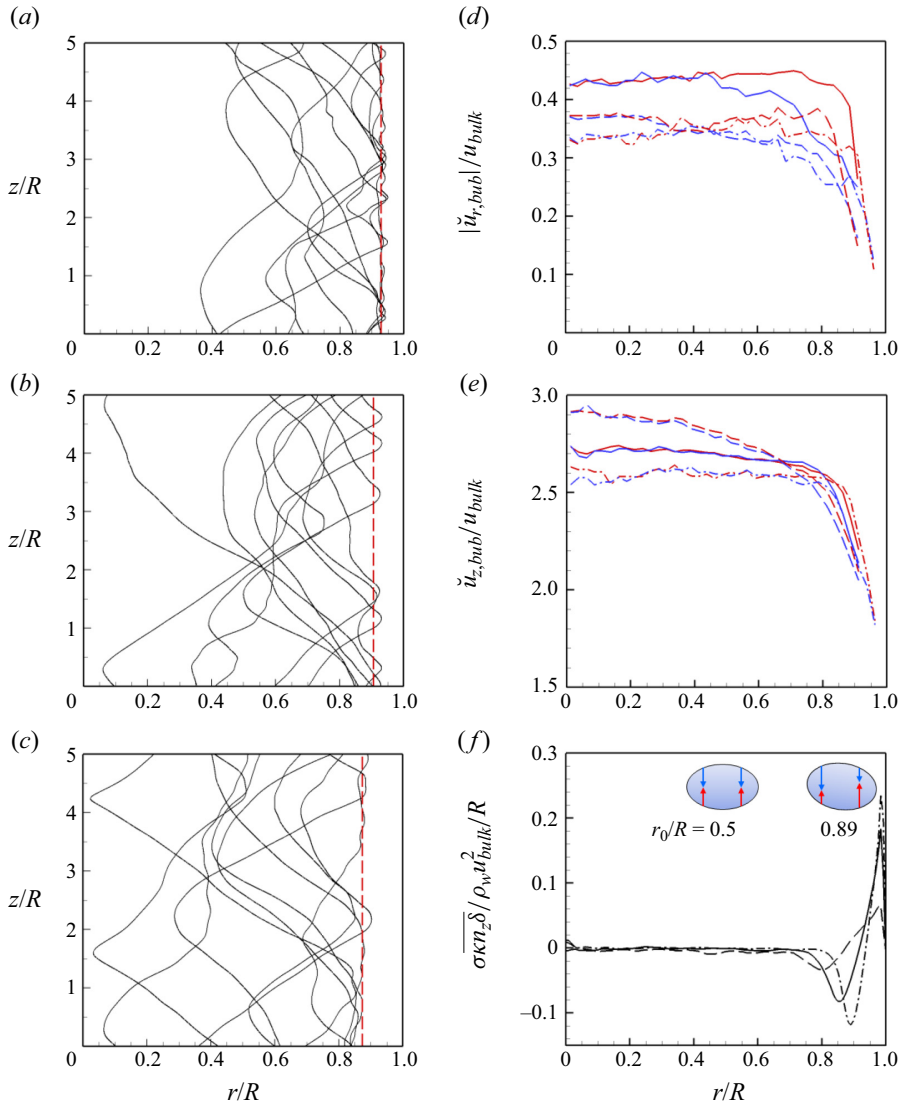


Figure 16. Bubble trajectories, conditional mean bubble velocities and mean surface: (a–c) bubble trajectories for cases SM, MM and LM, respectively; (d–e) conditional mean radial and axial bubble velocities ( $\dot{u}_{r,bub}$  and  $\dot{u}_{z,bub}$ ), respectively; (f) surface tension. In (a–c), each trajectory is obtained at a different time, and red dashed lines indicate the locations of  $r = R - l_{bub}(r)$ , where  $l_{bub}(r)$  is the mean major axis length of bubbles. In (d,e), the red and blue colours denote the mean bubble velocities moving towards the wall and centre, respectively (dot-dashed, case SM; solid, MM; dashed, LM). In (f), the mean bubble shapes observed at  $r_0/R = 0.5$  and  $0.89$  (case MM) are also shown (their aspect ratios are 1.81 and 1.52, respectively), where red and blue arrows denote the positive and negative axial directions of the surface tension at four locations of the upper and lower bubble surfaces, respectively, and their lengths represent the magnitudes.

movement direction owing to the drag force exerted on the bubble. Thus, near the wall, bubbles moving to the wall are tilted in the clockwise direction, and those moving away from the wall are tilted in the counter-clockwise direction. Since a bubble moving to the wall has stronger radial velocity, the mean bubble shape near the wall is rotated in the clockwise direction. Away from the wall, the radial velocities moving to and away from

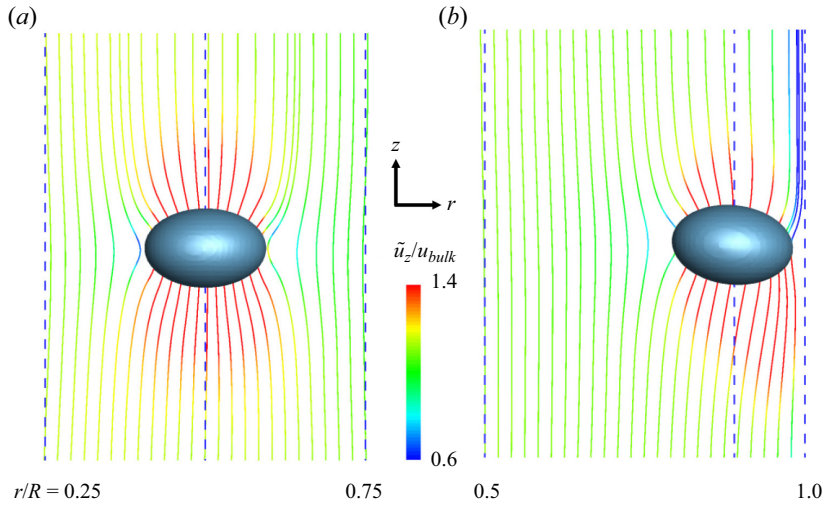


Figure 17. Mean shapes of the bubbles located at  $|r - r_o| \leq 0.5\Delta r$  ( $\Delta r = 0.0039D$ ), and surrounding mean streamlines coloured by the contours of the conditionally averaged mean axial velocity (case MM): (a)  $r_o/R = 0.5$ ; (b)  $r_o/R = 0.89$ .

the wall are nearly the same, and thus the major axis of the mean bubble shape is parallel to the horizontal plane.

Figure 17 shows the mean bubble shapes located at  $r_o/R = 0.5$  and  $0.89$ , and surrounding mean streamlines coloured by the contours of the conditionally averaged mean axial velocity for case MM. The mean bubble shapes are reconstructed from their mean vertical angles and lengths of major and minor axes. Their aspect ratios and inclination angles of the minor axis from the vertical direction are  $AR = 1.81$  and  $1.52$  and  $\theta_i = 0$  and  $6.08^\circ$ , respectively, for the bubbles located at  $r_o/R = 0.5$  and  $0.89$ . The conditionally averaged mean velocity  $\tilde{\mathbf{u}}$  is obtained by averaging the instantaneous water velocity fields around bubbles located at  $|r - r_o| \leq 0.5\Delta r$ . The distribution of the mean streamlines around the bubble located at  $r_o/R = 0.5$  is nearly axisymmetric about the vertical axis (this tendency is observed for the bubbles located at  $r_o/R < 0.8$ ). On the other hand, the bubble located at  $r_o/R = 0.89$  and surrounding mean streamlines are asymmetric due to the presence of the wall, as discussed above. When a bubble is located near the wall (figure 17b), the mean streamlines are more asymmetric with respect to the major axis on the wall side than on the centre side (in other words, more acceleration and deceleration of the axial velocity behind and in front of the bubble on its wall side, respectively), which significantly increases the r.m.s. axial velocity fluctuations very near the wall (figure 11c).

The distributions of the mean axial surface tension in the radial direction are shown in figure 16(f) for cases SM, MM and LM, together with schematic diagrams of mean bubble shapes located at  $r_o/R = 0.5$  and  $0.89$ . In the centre region, the axial surface tension is close to zero because the major axis of the mean bubble shape there is nearly perpendicular to the axial direction (like the mean bubble at  $r_o/R = 0.5$ ) and thus the integral of the surface tension along the bubble surface at each radial location in this region is nearly zero. On the other hand, when the major axis of a bubble is tilted like the mean bubble at  $r_o/R = 0.89$ , the curvatures ( $\kappa$ ) and angles between the surface-normal and axial directions ( $\eta = \cos^{-1}(\mathbf{n} \cdot \mathbf{k})$ ) vary along the bubble surface at each radial location. Then, on the left-hand side (towards the centre) of a bubble, the upper surface has a higher  $\kappa$  and a smaller  $\eta$  than the lower surface, resulting in surface tension in the negative axial direction. Likewise,

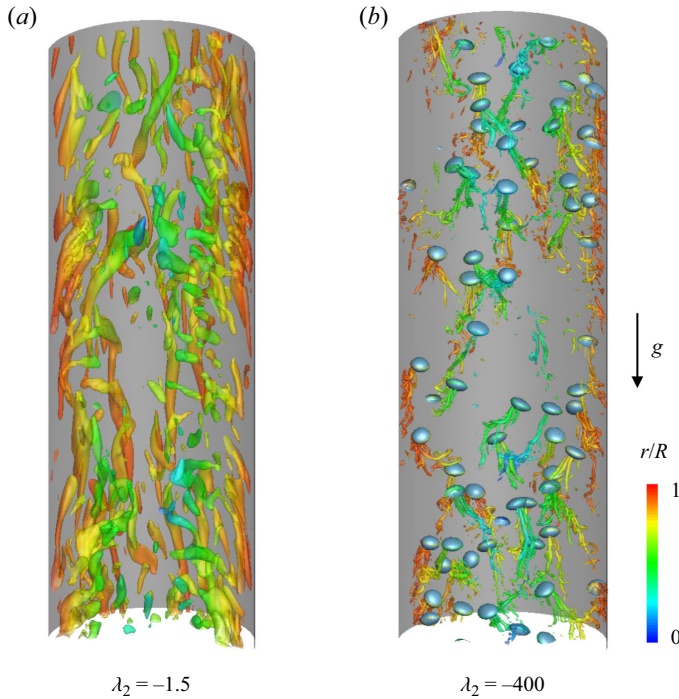


Figure 18. Instantaneous vortical structures identified by the iso-surfaces of  $\lambda_2$  (Jeong & Hussain 1995) coloured by the radial position: (a) single-phase flow; (b) bubbly flow (case MM). In (b), the bubble surfaces are identified by the iso-surfaces of  $\psi = 0.5$ .

the right-hand side (towards the wall) of a bubble has surface tension in the positive axial direction (see the magnitudes of blue and red arrows on the mean bubble shape at  $r_o/R = 0.89$  in figure 16f). According to this radial distribution of the surface tension ( $\sigma \kappa n_z \delta$ ), the surface tension term in (3.4), which is the integral of surface tension in the radial direction, is nearly zero in the centre region, negative near the wall, and zero at the wall (see figure 14).

Figure 18 shows the instantaneous vortical structures for the single-phase and bubbly (case MM) flows, coloured by their radial position. Note that a much higher value of  $|\lambda_2|$  is used for the bubbly flow because bubble-induced vortices are much stronger than shear-induced vortices. The length scales of these vortices in the bubbly flow are smaller than those in the single-phase flow. It is noteworthy that near-wall coherent structures observed in wall-bounded turbulent flow nearly disappear in the bubbly flow, and most strong vortices are found in the wake behind bubbles. As bubbles are distributed over the whole radial locations (see figure 9), the vortices are observed everywhere in the pipe.

Figure 19 shows the instantaneous vortical structures at  $r/R < 0.8$ , coloured by the contours of the instantaneous axial vorticity for cases SM ( $d_{eq}/D = 0.0655$  and  $Re_{bub} = 533$ ), MM ( $d_{eq}/D = 0.0825$  and  $Re_{bub} = 737$ ) and LM ( $d_{eq}/D = 0.1040$  and  $Re_{bub} = 1000$ ). Note that the region of  $r/R < 0.8$  is chosen where the relative bubble velocities are nearly uniform (see figure 10b). The vortices behind each bubble in figure 19 are qualitatively similar to those behind a freely rising air bubble at a similar  $Re_{bub}$  (Brücker 1999; De Vries, Biesheuvel & Van Wijngaarden 2002). For case SM (figure 19a), the wake behind a bubble consists of double-threaded vortices (denoted as a dashed ellipse) that primarily convey the axial vorticity. For case MM (figure 19b), the wake



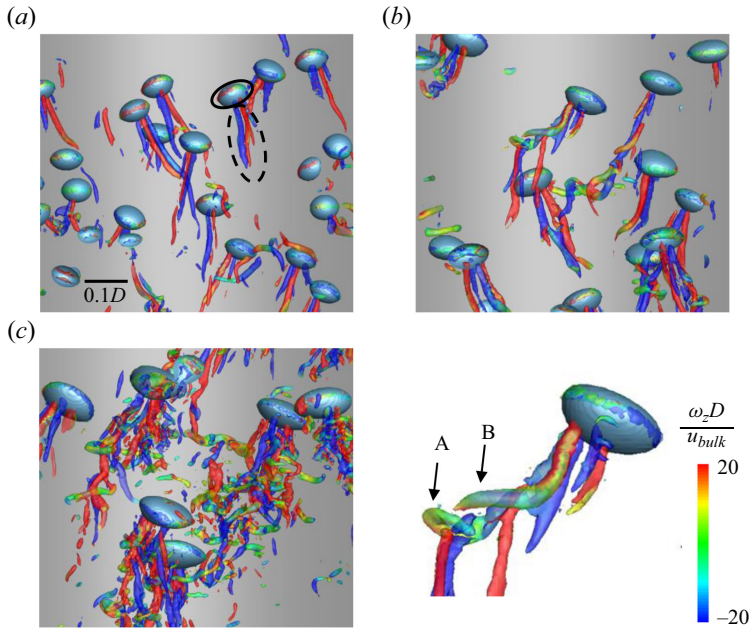


Figure 19. Instantaneous vortical structures (identified by  $\lambda = -400$ ) at  $r/R < 0.8$  coloured by the contours of the instantaneous axial vorticity  $\omega_z$ : (a)  $d_{eq}/D = 0.0655$  (SM); (b)  $d_{eq}/D = 0.0825$  (MM); (c)  $d_{eq}/D = 0.1040$  (LM). Here, the bubble surfaces are identified by the iso-surfaces of  $\psi = 0.5$ . Thick solid and dashed ellipses in (a) indicate toroidal and double-threaded vortices, respectively. Below (b), one-sided hairpin vortices ('A' and 'B') in the wake of a bubble are identified for case MM.

consists of not only double-threaded vortices but also hairpin vortices (shown below panel (b)) that carry the horizontal vorticity components as well as the axial one. Symmetric hairpin vortices are often observed in the wake of a single bubble rising in a zigzag trajectory (Brücker 1999). For the present flow, hairpin vortices in the wake of bubbles are predominantly one-sided (i.e. one-legged) rather than symmetric (two-legged) because of complex interactions among bubbles and their wake. For case LM (figure 19c), the wake contains a bunch of double-threaded and hairpin vortices. These vortices are denser and more irregular than those observed from case MM. A toroidal vortex is also observed inside bubble surfaces (denoted as a solid curve in figure 19a) for all the cases considered (see below for details).

Figure 20 shows the instantaneous wall shear stress for the single-phase and bubbly flows (cases SM, MM and LM). Note that the mean wall shear stresses of cases SM, MM and LM are 3.22, 2.51 and 2.02 times that of the single-phase flow, respectively (table 1). The streaky structure of the wall shear stress observed for the single-phase flow does not exist, but spotty structures are found in the bubbly flows. As  $d_{eq}$  increases, the spotty structure occurs less frequently but increases in size.

Figure 21 shows the time sequence of a bubble near the wall and associated vortices for case MM, together with the contours of the wall shear stress beneath the bubble. At  $tu_{bulk}/D = 16.35$ , a bubble approaches the wall, and negative wall shear stress occurs behind the bubble. When a bubble moves upward and approaches the wall, an inclined stagnation flow is generated beneath the bubble, and a reverse flow region is formed just under the bubble, as shown in figure 22, resulting in a negative wall shear stress region there. Note also that a toroidal vortex is generated inside the bubble and the direction



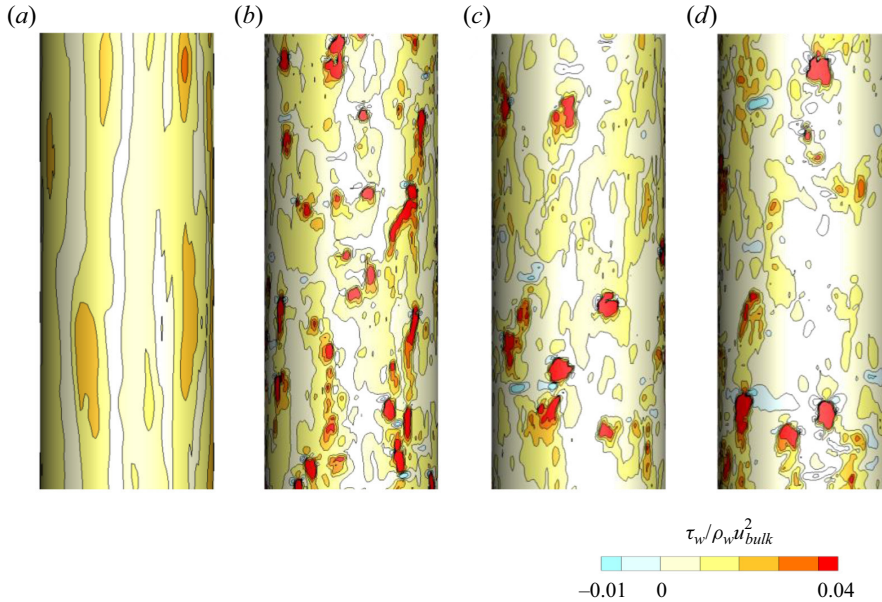


Figure 20. Contours of the instantaneous wall shear stress: (a) single-phase flow; (b) case SM; (c) MM; (d) LM.

of rotation of this vortex near the wall is same as that of the velocity field under the bubble (see [figure 22](#)). During wall–bubble collision ( $tu_{bulk}/D = 16.40$ ), regions of high wall shear stress occur beneath and behind the bubble owing to its sweeping motion towards the wall and the wall-ward velocity induced by a pair of counter-rotating vortices behind the bubble, respectively. This pair of vortices are generated by the interaction of the bubble with the wall (see these vortices very near the wall from  $(z, r)$  plane view at  $tu_{bulk}/D = 16.40$ ). This pair of vortices further develops as the bubble bounces off the wall and creates a region of longer high wall shear stress ( $tu_{bulk}/D = 16.50$ ). Note that, at this instant, the signs of counter-rotating vortices are opposite to those at  $tu_{bulk}/D = 16.35$  (this is very different from those of bouncing counter-rotating vortices behind a bubble in still water (Lee & Park 2017)), and the velocity induced by these vortices in the wake pushes the bubble away from the wall. However, at  $tu_{bulk}/D = 16.70$ , the bubble moves towards the wall again by the high shear near the wall, and generates a new pair of near-wall counter-rotating vortices right behind the bubble, resulting in high skin friction there. Note that a pair of long counter-rotating vortices behind the bubble are generated from the wall-ward motion of the bubble and has opposite signs of rotation to those generated from the interaction with the wall. Also, the region of the high wall shear stress and near-wall vortices created during  $tu_{bulk}/D = 16.40$ – $16.50$  persist at  $tu_{bulk}/D = 16.70$ , although the corresponding bubble moves away from these flow structures. These vortical structures near the wall significantly increase the mean skin friction and r.m.s. velocity fluctuations very near the wall ([figure 11](#)). Lu & Tryggvason (2008, 2013) numerically observed for a density ratio of  $\rho_{bubble}/\rho_{liquid} = 0.1$  that most bubbles slide along the channel walls and form a cluster for wall-peaking turbulent bubbly channel flows. This difference in bubble–wall interactions may come from very different density ratios considered. [Figure 23](#) shows the instantaneous vortical structure around bouncing-off bubbles for cases SM, MM and LM. As  $d_{eq}$  increases, the vortices generated by the interaction of the

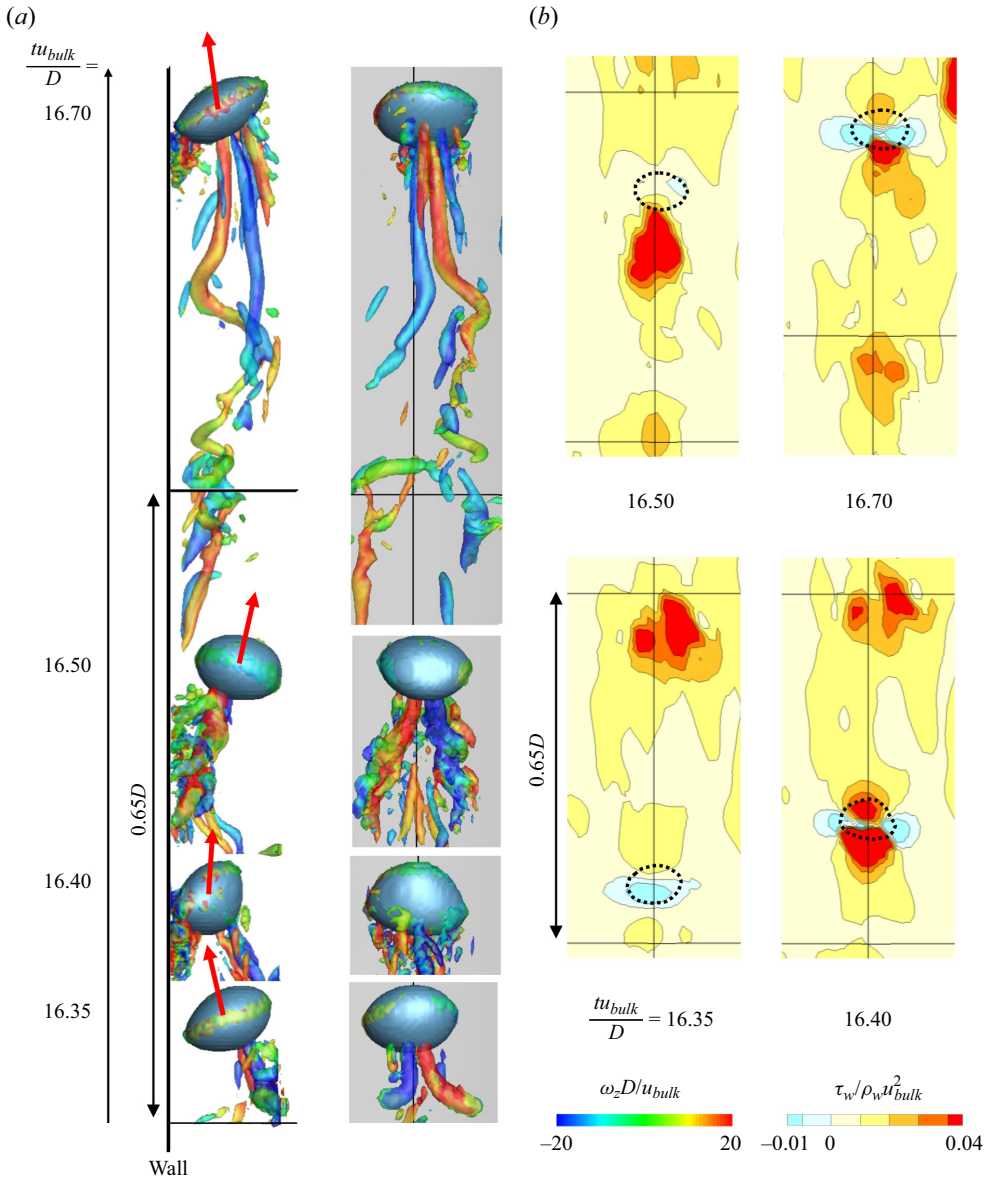


Figure 21. Time sequence of a bubble near the wall and associated vortices coloured by the contours of the instantaneous axial vorticity, and contours of the instantaneous wall shear stress beneath the bubble (case MM): (a) (left)  $(z, r)$  and (right)  $(z, \theta)$  plane views; (b) wall shear stress. Here, the bubble surfaces are identified by the iso-surfaces of  $\psi = 0.5$ . In (a), red arrows represent the instantaneous bubble velocities. In (b), dotted circles indicate the locations of the bubble projected on the wall.

bubble with the wall become stronger and more complex. Nevertheless, the most important vortices are the pair of counter-rotating vortices that induce high-speed water flow towards the wall and create high wall shear stress, as discussed in figure 21.

Figure 24 shows the PDFs of the directional angle ( $\alpha$ ) of the bubble velocity vector deviated from the axial direction for the bubbles located at  $0.45 < r/R < 0.50$  and  $0.85 < r/R < 0.90$  (cases ML, MM and MH). Here, the PDF is obtained

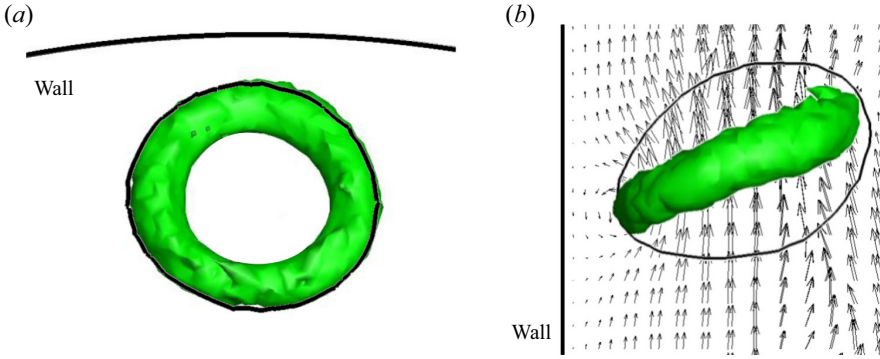


Figure 22. A bubble approaching wall and nearby velocity field, together with a toroidal vortex inside the bubble at  $tu_{bulk}/D = 16.35$  (case MM): (a) top view; (b) side view. Here, the bubble surface (thin black circle) and toroidal vortex (green colour) are identified by the iso-surfaces of  $\psi = 0.5$  and  $\lambda_2 = -1875$ , respectively.

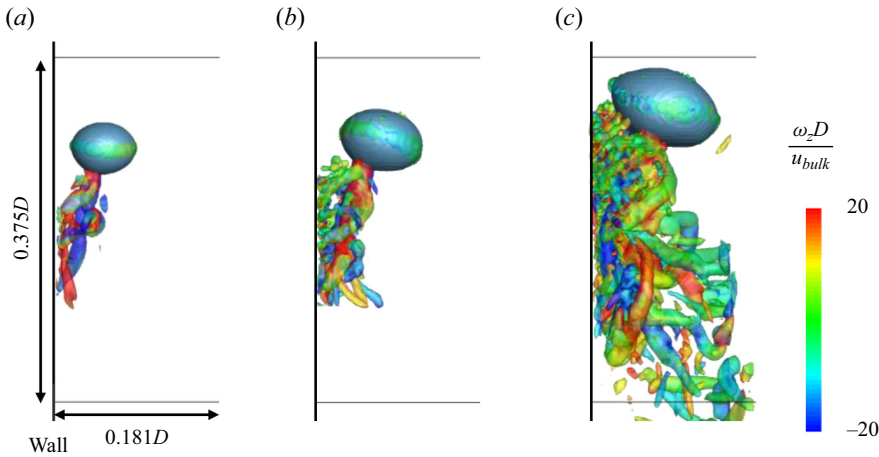


Figure 23. Instantaneous vortical structures (identified by  $\lambda = -400$ ) behind a bouncing-off bubble coloured by the contours of the instantaneous axial vorticity  $\omega_z$ : (a)  $d_{eq}/D = 0.0655$  (case SM); (b)  $d_{eq}/D = 0.0825$  (case MM); (c)  $d_{eq}/D = 0.1040$  (case LM). Here, the bubble surfaces are identified by the iso-surfaces of  $\psi = 0.5$ . The bubble radial locations are  $r_o = 0.855, 0.845$  and  $0.849R$  for cases SM, MM and LM, respectively.

as  $PDF(\alpha_o, \theta_o) = N(|\alpha - \alpha_o| \leq \Delta\alpha/2, |\theta - \theta_o| \leq \Delta\theta/2) / \{N(0^\circ \leq \alpha \leq 180^\circ, 0^\circ \leq \theta \leq 360^\circ) \times \sin \alpha \Delta\alpha \Delta\theta\}$ , where  $N(\cdot)$  is the number of events,  $\Delta\alpha = 1.41^\circ$  and  $\Delta\theta = 5.63^\circ$ . No bubble is observed to move downward, and thus the directional angles of  $0^\circ \leq \alpha \leq 90^\circ$  are drawn in this figure. When bubbles move homogeneously in  $0^\circ \leq \alpha \leq 90^\circ$ , the magnitude of the PDF is constant ( $= 1/(2\pi) = 0.159$ ). For the bubbles located at  $0.45 < r/R < 0.50$  (top panels in figure 24a–c), the contours of the PDF are nearly axisymmetric, indicating that there is no preferred horizontal movement direction and bubbles located away from the wall are little affected by the pipe wall. However, the PDFs have clear peaks at  $\alpha \approx 16^\circ, 14^\circ$  and  $10^\circ$  for cases ML, MM and MH, respectively. That is, as  $\langle \psi \rangle$  increases, more bubbles located at  $0.45 < r/R < 0.50$  move at a smaller directional angle from the vertical direction, and the PDF at  $\alpha = 0^\circ$  increases. Now, let us consider the bubbles located at  $0.85 < r/R < 0.90$  where  $\bar{\psi}$  is high (figure 9). At this radial location (bottom panels in figure 24a–c), the contours of the PDF are asymmetric and inclined

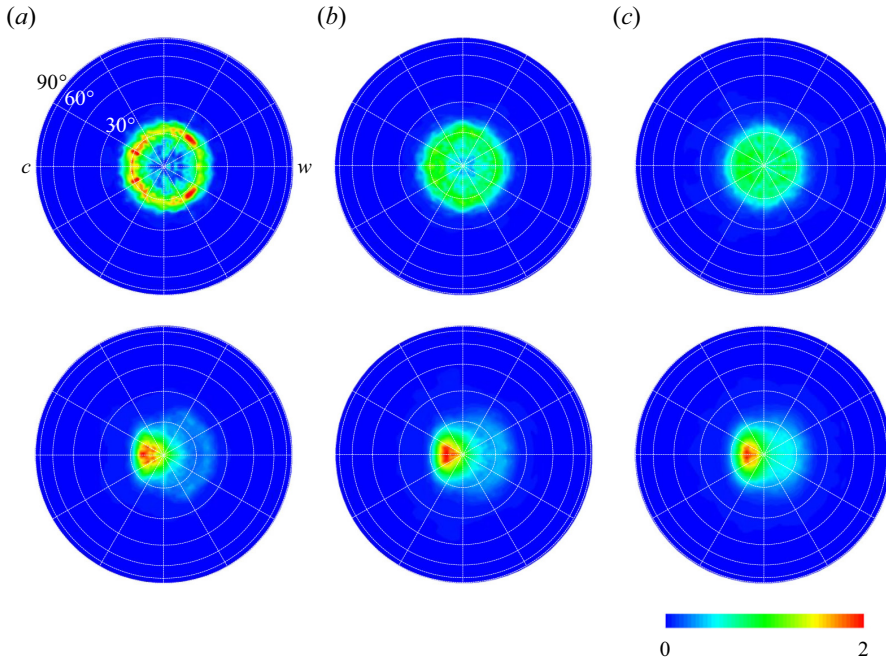


Figure 24. PDFs of the directional angle of the bubble velocity vector deviated from the axial direction for the bubbles located at  $0.45 < r/R < 0.50$  (top) and  $0.85 < r/R < 0.90$  (bottom): (a) case ML; (b) MM; (c) MH. Here, ‘c’ and ‘w’ denote the directions towards the pipe centre and wall from a bubble location, respectively.

towards the pipe centre. The most preferred directional angles are  $\alpha \approx 9^\circ, 8^\circ$  and  $7^\circ$  towards the pipe centre for cases ML, MM and MH, respectively. Note also that there are clear second peaks of the PDF (arc-shaped contours in this figure) at  $\alpha \approx 19^\circ, 17^\circ$  and  $13^\circ$  towards the wall region for cases ML, MM and MH, indicating that the wall-approaching angle of bubbles is statistically larger than the bounce-off angle.

#### 4. Conclusions

In the present study, we investigated the turbulence characteristics, bubble behaviour and vortical structures in an air–water upward bubbly pipe flow at  $Re_{bulk} = 5300$  and  $Re_{pub} = 533\text{--}1000$  using a high-resolution numerical simulation. A single-phase flow and five monodispersed bubbly flows with varying bubble equivalent diameter ( $d_{eq} = 2.62, 3.30, 4.16$  mm) and total bubble volume fraction ( $\langle \bar{\psi} \rangle = 0.75\%, 1.5\%, 3.0\%$ ) were examined. Flat and wall-peaking bubble distributions were observed, respectively, for the case with the largest  $d_{eq}$  ( $= 4.16$  mm) and the other four cases. These radial bubble distributions significantly affected the turbulence statistics of bubbly flows.

As the bubble concentration near the wall increased with increasing total bubble volume rate and decreasing bubble equivalent diameter, the mean shear rates near and at the wall increased significantly. The profiles of the r.m.s. velocity fluctuations of the bubbly flows were proportional to  $\bar{\psi}^{0.4}$  ( $\bar{\psi}(r)$  is the mean bubble volume fraction), which is a characteristic of bubble-induced turbulence as observed for homogeneous bubbly flows by Risso & Ellingsen (2002) and Riboux *et al.* (2010). This result indicated that shear-induced turbulence was suppressed in the present bubbly flows. The vortices in the bubbly flows were smaller in size but denser and more intense than those in

the single-phase flow. Consequently, the bubble-induced vortices were strong enough to hinder the development of shear-induced vortices, and the velocity fluctuations primarily exhibited the characteristics of bubble-induced turbulence. The Reynolds shear stress was analysed considering the balance among the viscous shear stress, mean pressure gradient, gravitational force and surface tension in the Reynolds-averaged axial momentum equation. The Reynolds shear stress around the pipe centre mainly came from the positive mean pressure gradient and negative gravitational force, while those near the wall came from the positive gravitational force and negative surface tension in addition to the positive mean pressure gradient. The positive and negative peaks of the surface tension near the wall were caused by the stronger bubble motion towards the wall and tilted bubble shape. Bubbles near the wall approached and bounced off the wall. After collision with the wall, counter-rotating vortices in the wake of bubbles were generated and increased the skin friction. As the bubble equivalent diameter increased, they became more tilted and complicated, and induced higher water velocity to the wall.

We suggested a modified algebraic RANS model based on the interaction between shear-induced and bubble-induced turbulence. Unlike the previous RANS model of Sato *et al.* (1981a), the present one considered relative strengths of these types of turbulence. The present model showed a better performance than the previous one at a wide range of the water bulk Reynolds number.

**Funding.** This work was supported by the National Research Foundation of Korea (nos. 2017M2A84018482 and 2021R1A4A1032023). The computer resources were provided by the KISTI Super Computing Center (no. KSC-2020-CRE-0228).

**Declaration of interests.** The authors report no conflict of interest.

**Author ORCIDs.**

 Haecheon Choi <https://orcid.org/0000-0003-0696-847X>.

## Appendix A. Numerical methods

Equations (2.1) and (2.2) are solved using a semi-implicit four-step fractional-step method:

$$\frac{\hat{\rho} - \rho^{k-1}}{2\alpha_k \Delta t} = -\frac{\beta_k}{2\alpha_k} \nabla \cdot (\rho_f^{k-1} \mathbf{u}^{k-1}) - \frac{\gamma_k}{2\alpha_k} \nabla \cdot (\rho_f^{k-2} \mathbf{u}^{k-2}), \quad (\text{A1})$$

$$\begin{aligned} \frac{\hat{\rho} \hat{\mathbf{u}} - \rho^{k-1} \mathbf{u}^{k-1}}{2\alpha_k \Delta t} = & -\Pi^{k-1} \mathbf{k} - \nabla p^{k-1} + \frac{1}{2} \{L(\hat{\mu}, \hat{\mathbf{u}}) + L(\mu^{k-1}, \mathbf{u}^{k-1})\} \\ & + \frac{\beta_k}{2\alpha_k} N(\rho_f^{k-1}, \mu^{k-1}, \mathbf{u}^{k-1}) + \frac{\gamma_k}{2\alpha_k} N(\rho_f^{k-2}, \mu^{k-2}, \mathbf{u}^{k-2}) \end{aligned} \quad (\text{A2})$$

$$+ \left\{ \frac{1}{2} (\hat{\rho} + \rho^{k-1}) - \langle \rho \rangle \right\} \mathbf{g} + \sigma \kappa^{k-1} \delta^{k-1} \mathbf{n}^{k-1} + \mathbf{f}^k,$$

$$\frac{\hat{\rho} \mathbf{u}^* - \hat{\rho} \hat{\mathbf{u}}}{2\alpha_k \Delta t} = \Pi^{k-1} \mathbf{k} + \nabla p^{k-1}, \quad (\text{A3})$$

$$\nabla \cdot \left( \frac{1}{\hat{\rho}} (\Pi^k \mathbf{k} + \nabla p^k) \right) = \frac{1}{2\alpha_k \Delta t} \nabla \cdot \mathbf{u}^*, \quad (\text{A4})$$

$$\frac{\hat{\rho} \mathbf{u}^k - \hat{\rho} \mathbf{u}^*}{2\alpha_k \Delta t} = -\Pi^k \mathbf{k} - \nabla p^k, \quad (\text{A5})$$



where

$$L(\mu, \mathbf{u}) = \nabla \cdot (\mu \nabla \mathbf{u}) + \nabla \cdot \mathbf{D}(\mu \nabla^T \mathbf{u}), \quad (\text{A6})$$

$$N(\rho, \mu, \mathbf{u}) = -\nabla \cdot (\rho \mathbf{u} \mathbf{u}) + \nabla \cdot \mathbf{N} \mathbf{D}(\mu \nabla^T \mathbf{u}), \quad (\text{A7})$$

$\hat{\rho}$  is the provisional density obtained by (A1),  $\rho_f (= \rho_a \psi_\Gamma + \rho_w(1 - \psi_\Gamma))$  is an upwind-type flux density defined at a cell face,  $\psi_\Gamma$  is the bubble volume fraction of the region  $\Gamma$  that contains fluids passing through the cell face during  $\beta_k \Delta t$  at  $t = t^{k-1}$  (for  $\rho_f^{k-1}$ ) or  $\gamma_k \Delta t$  at  $t = t^{k-2}$  (for  $\rho_f^{k-2}$ ),  $\hat{\mu}$  is the viscosity calculated from (2.4) with  $\hat{\rho}$  and  $\psi$  obtained by (A1) and (2.3), respectively,  $\hat{\mathbf{u}}$  and  $\mathbf{u}^*$  are the intermediate velocities,  $\mathbf{D}(T)$  and  $\mathbf{N} \mathbf{D}(T)$  are the tensors consisting of diagonal and non-diagonal elements of tensor  $T$ , respectively, and the subscript  $k$  ( $= 1, 2, 3$ ) is the sub-time-step index ( $\alpha_1 = 4/15$ ,  $\alpha_2 = 1/15$ ,  $\alpha_3 = 1/6$ ,  $\beta_1 = 8/15$ ,  $\beta_2 = 5/12$ ,  $\beta_3 = 3/4$ ,  $\gamma_1 = 0$ ,  $\gamma_2 = -17/60$ ,  $\gamma_3 = -5/12$ ). Here, a third-order Runge–Kutta method is applied to the convection and non-diagonal viscous terms, and the Crank–Nicolson method is applied to the viscous (excluding non-diagonal term) and gravitational terms. An explicit Euler method is used for the surface tension term to achieve a discrete balance between the surface tension and pressure gradient forces (Kim 2011). The second-order central difference method is used for all spatial derivative terms except for the convection terms at the phase interface cell in (A1) and (A2) where an upwind-type mass-flux method (Kim 2011; Kim & Choi 2018) is used. These consistent temporal and spatial discretization methods adopted for the convection terms in (A1) and (A2) ensure an accurate momentum transport, which is crucial for the present simulation of two-phase flow with a high density ratio ( $\rho_w/\rho_a \approx 1000$ ) (Raessi & Pitsch 2012).

A multigrid preconditioned conjugate gradient method (Tatebe 1993) is used to solve the variable-coefficient Poisson equation (A4). Approximately 20 iterations are needed to satisfy a convergence criterion of  $|\nabla \cdot \mathbf{u}|_{\max} < 10^{-6}$ , which consumes approximately 40 % of the whole computational time. The size of the computational time step is restricted by the conventional Courant–Friedrichs–Lewy (CFL) condition on the convective term ( $\text{CFL}_{\max} \leq \sqrt{3}$ ) and also by the capillary time-step constraint induced by the explicit treatment of the surface tension term (Brackbill, Kothe & Zemach 1992):

$$\Delta t \leq \sqrt{\frac{(\rho_a + \rho_w) \Delta x_{\min}^3}{4\pi\sigma}}, \quad (\text{A8})$$

where  $\Delta x_{\min}$  is the smallest grid size. For the present problem, the computational time step is mostly bounded by (A8).

Equation (2.5) is solved using a third-order total variation diminishing (TVD) Runge–Kutta method (Gottlieb & Shu 1998) and a fifth-order weighted essentially non-oscillatory (WENO) scheme in conjunction with a local Lax–Friedrichs entropy correction (Jiang & Peng 2000) for temporal and spatial discretizations, respectively. To maintain the signed-distance property, the level-set function is reinitialized at every other time step by solving the following partial differential equation (Sussman, Smereka & Osher 1994; Peng *et al.* 1999):

$$\frac{\partial \phi}{\partial \tau_r} + \frac{\phi}{\sqrt{\phi^2 + |\nabla \phi|^2 \Delta x_\phi^2}} (|\nabla \phi| - 1) = 0, \quad (\text{A9})$$

where  $\tau_r$  is the pseudo-time for the reinitialization iteration and  $\Delta x_\phi$  is the level-set grid size. Equation (A9) is iteratively solved using a third-order TVD Runge–Kutta method in



time and a fifth-order WENO scheme with a Godunov flux scheme in space. The volume of each bubble is conserved by relocating the phase interface from

$$\frac{\partial \phi}{\partial \tau_v} = \frac{\phi}{\sqrt{\phi^2 + |\nabla \phi|^2 \Delta x_\phi^2}} \frac{V_b(t) - V_b(t=0)}{V_b(t=0)}, \quad (\text{A10})$$

where  $\tau_v$  is the pseudo-time for the volume correction iteration and  $V_b$  is the bubble volume (Son 2001; Zhang *et al.* 2010). We assign a level-set function to each bubble to avoid numerical coalescence (Coyajee & Boersma 2009). Each level-set function is solved in the cuboid which contains a bubble and at least six grid points outside the bubble interface. When a bubble locates very near the pipe wall, only the level-set grid points located inside the pipe are used to solve (2.5). If a bubble penetrates the pipe wall, a special treatment is required. However, this did not occur at all (because of the velocity distribution very near the wall) during  $tu_{bulk}/D = 10$  for all cases considered, and thus such a treatment was not needed.

According to Sanada *et al.* (2009), bubbles in water coalesce at  $Re_{bub} < 540$ –590. Among the cases considered, the bubble Reynolds number of case SM ( $Re_{bub} = 533$  and  $d_{eq} = 2.62$  mm; see table 1) is within this criterion. However, the bubble volume fraction of case SM is only  $\langle \psi \rangle = 1.5\%$  and thus the possibility of bubble collisions must be very low. Riboux *et al.* (2010) also indicated that bubble coalescence was not observed in a homogeneous bubbly flow for  $d_{eq} = 1.6, 2.1$  and 2.5 mm and  $\langle \psi \rangle = 0.5\%$ –10%. Therefore, for all the cases considered in the present study, we expect that bubble coalescence does not occur or little affects the flow fields even if it happens.

When bubbles approach very closely to the wall and rebound from the wall, a thin liquid film is formed and thus resolving this thin film is required. Typically, the number of grid points within this liquid film (for the Navier–Stokes equations) can reach one or two during simulation. Nevertheless, the time period of having one or two grids within thin film is very short ( $tu_{bulk}/D \approx 0.03$ ) because of the upward water flow and repulsive force from the wall, and thus numerical errors may not be noticeably accumulated during bubble–wall interactions. Albadawi *et al.* (2014) conducted numerical simulations for a bouncing bubble from a horizontal surface with and without mesh refinement near the wall. The results with mesh refinement (having a mesh size smaller than liquid film thickness) were better than those without mesh refinement (mesh size was about 50 times that of refined mesh). However, the simulation without mesh refinement still captured the temporal variation of the bubble velocity during four rebounding periods. The use of adaptive mesh reported recently (Innocenti *et al.* 2021; Yan *et al.* 2022) will further improve the numerical accuracy during this time period.

## Appendix B. A modified algebraic RANS model

In this appendix, we revisit the algebraic model by Sato *et al.* (1981a) for the predictions of the wall shear stress and mean axial velocity profile, and suggest a revised model by introducing the effect of the interaction between the shear-induced and bubble-induced turbulence.

Sato *et al.* (1981a) provided the following equation for the mean velocity gradient in a pipe assuming that the dispersed gas phase is void:

$$\frac{d\bar{u}_z}{dr} = \frac{1}{\rho_w(1 - \bar{\psi})(\nu_w + \nu_t)} \left\{ \frac{r}{R} \left( -\tau_w + \frac{\rho_w g}{R} \int_0^R \bar{\psi} r dr \right) - \frac{\rho_w g}{r} \int_0^r \bar{\psi} r dr \right\}, \quad (\text{B1})$$

with

$$v_t(r) = v_{SIT}(r) + v_{BIT}(r), \quad (\text{B2})$$

$$v_{SIT}(r) = k_0 v_w C_r \left\{ 1 - \frac{11}{6} \left( \frac{R-r}{R} \right) + \frac{4}{3} \left( \frac{R-r}{R} \right)^2 - \frac{1}{3} \left( \frac{R-r}{R} \right)^3 \right\} (R^+ - r^+), \quad (\text{B3})$$

$$v_{BIT}(r) = \frac{1}{2} k_1 C_r \hat{d}_{eq} \bar{\psi} (u_{bub} - u_{bulk}) \approx \frac{1}{2} k_1 C_r \hat{d}_{eq} \bar{\psi} u_T, \quad (\text{B4})$$

where  $v_w$  is the water kinematic viscosity,  $v_t$  is the turbulent kinematic viscosity decomposed into the shear-induced ( $v_{SIT}$ ) and bubble-induced ( $v_{BIT}$ ) kinematic viscosities,  $C_r = (1 - \exp(-(R^+ - r^+)/A^+))^2$ ,  $r^+ = ru_\tau/\nu_w$ ,  $R^+ = Ru_\tau/\nu_w$ ,  $u_\tau = \sqrt{\tau_w/\rho_w}$ ,  $A^+ (= 16)$  is the van Driest (1956) damping factor coefficient,  $k_0 (= 0.4)$  and  $k_1 (= 1.2)$  are empirical constants and  $\hat{d}_{eq} = d_{eq}$  for  $0 \leq r < R - d_{eq}/2$  and  $4(R-r)(d_{eq} - (R-r))/d_{eq}$  for  $R - d_{eq}/2 \leq r \leq R$ . Since the relative bubble velocity,  $u_{bub} - u_{bulk}$ , in (B4) is unknown *a priori*, the mean terminal velocity of rising bubbles ( $u_T$ ) was used instead of  $u_{bub} - u_{bulk}$ . For the present computations, we obtain  $u_T$  from the plot of  $d_{eq}$  versus  $u_T$  in Clift, Grace & Weber (2005). Note that  $v_{SIT}$  in (B3) is based on single-phase turbulent pipe flow. Also, the radial distribution of  $\bar{\psi}(r)$  has to be given *a priori* to solve (B1).

In §§ 3.1 and 3.2, we observed that bubble-induced turbulence hinders the development of shear-induced turbulence when the vorticity magnitude of bubble-induced turbulence is much larger than that of shear-induced turbulence (see figures 18 and 11). However, the model suggested by Sato *et al.* (1981a) contains both characteristics irrespective of the relative strength of both turbulence types. Therefore, the turbulent kinematic viscosity is modified by introducing  $\chi$  as follows:

$$v_t(r) = (1 - \chi)v_{SIT}(r) + \chi v_{BIT}(r), \quad (\text{B5})$$

with

$$\chi = \exp(-k_2 u_{bulk}/(u_{bub} - u_{bulk})) \approx \exp(-k_2 u_{bulk}/u_T), \quad (\text{B6})$$

where  $\chi$  is the fraction of bubble-induced turbulence ( $0 \leq \chi \leq 1$ ). The empirical constants  $k_1$  and  $k_2$  in (B4) and (B6) are determined by an iterative method such that the predicted wall shear stresses match those of case 2 (from present simulation) and case 14 (from an experiment by Liu (1997)). These two cases correspond to the smallest and largest water bulk velocities investigated in the present study, respectively (see table 4). As a result, we obtain  $k_1 = 13.1$  and  $k_2 = 0.359$ , and use them for the prediction. We note that there may be a better representation of  $\chi$  by introducing more variables such as  $R/d_{eq}$ ,  $Re_{bub}$ ,  $Re_{bulk}$ , etc. However, we do not pursue this issue further because the present definition of  $\chi$  can successfully predict the wall shear stress for the cases considered.

Table 3 shows the computational procedure to obtain the mean axial velocity and wall shear stress using the present algebraic RANS model. The number of grid points in the radial direction is 201, where the smallest and largest grid spacings are  $\Delta r/R = 0.001$  at the wall ( $r = R$ ) and 0.028 at the centre ( $r = 0$ ), respectively. We use the trapezoidal method for numerical integrations in Steps 4 and 5. Term  $\mathcal{D}u_{bulk}/\mathcal{D}\tau_w$  in Step 6 is obtained as follows. From (B1) together with  $u_{bulk} = 2 \int_0^R \bar{u}_z(r)r dr/R^2$ , one can express  $u_{bulk}$  as a

- Step 0 Provide  $R, d_{eq}, u_{bulk}, \bar{\psi}(r)$  and properties of fluids.  
 Step 1 Assume  $\tau_w^0$ .  
 Step 2 Compute  $v_{SIT}^l(r)$  and  $v_{BIT}^l(r)$  from (B3) and (B4).  
 Step 3 Compute  $v_t^l(r)$  from (B5).  
 Step 4 Obtain  $\bar{u}_z^l(r)$  by integrating (B1) with  $\bar{u}_z(r=R)=0$ .  
 Step 5 Obtain  $u_{bulk}^l = 2 \int_0^R \bar{u}_z^l r \, dr / R^2$ .  
 Step 6 Update  $\tau_w^l = \tau_w^{l-1} - \frac{u_{bulk}^l - u_{bulk}}{\mathcal{D}u_{bulk}/\mathcal{D}\tau_w}|^l$ .  
 Step 7 If  $|u_{bulk}^l - u_{bulk}|/u_{bulk} > 10^{-6}$ , go to Step 2.  
 Otherwise,  $\bar{u}_z = \bar{u}_z^l$  and  $\tau_w = \tau_w^l$ .

Table 3. Iterative method to calculate the wall shear stress and mean axial velocity profile using the present RANS model. Here,  $l$  ( $= 1, 2, 3, \dots$ ) is the iteration index.

function of  $\tau_w$ :

$$\begin{aligned} u_{bulk}(\tau_w) = & -\frac{2\tau_w}{\rho_w R^3} \int_0^R r \int_R^r \frac{r'}{(1 - \bar{\psi}(r'))(v_w + v_t(\tau_w, r'))} \, dr' \, dr \\ & + \frac{2g}{R^4} \int_0^R \bar{\psi}(r'') r'' \, dr'' \int_0^R r \int_R^r \frac{r'}{(1 - \bar{\psi}(r'))(v_w + v_t(\tau_w, r'))} \, dr' \, dr \\ & - \frac{2g}{R^2} \int_0^R r \int_R^r \frac{1}{r'(1 - \bar{\psi}(r'))(v_w + v_t(\tau_w, r'))} \int_0^{r'} \bar{\psi}(r'') r'' \, dr'' \, dr' \, dr. \quad (B7) \end{aligned}$$

By taking the derivative of (B7) with respect to  $\tau_w$ , we obtain  $\mathcal{D}u_{bulk}/\mathcal{D}\tau_w$  as follows:

$$\begin{aligned} \frac{\mathcal{D}u_{bulk}}{\mathcal{D}\tau_w} = & -\frac{2}{\rho_w R^3} \int_0^R r \int_R^r \frac{r'}{(1 - \bar{\psi}(r'))(v_w + v_t(\tau_w, r'))} \, dr' \, dr \\ & + \frac{2\tau_w}{\rho_w R^3} \int_0^R r \int_R^r \frac{r' \mathcal{D}v_t(\tau_w, r')/\mathcal{D}\tau_w}{(1 - \bar{\psi}(r'))(v_w + v_t(\tau_w, r'))^2} \, dr' \, dr \\ & - \frac{2g}{R^4} \int_0^R \bar{\psi}(r'') r'' \, dr'' \int_0^R r \int_R^r \frac{r' \mathcal{D}v_t(\tau_w, r')/\mathcal{D}\tau_w}{(1 - \bar{\psi}(r'))(v_w + v_t(\tau_w, r'))^2} \, dr' \, dr \\ & + \frac{2g}{R^2} \int_0^R r \int_R^r \frac{\mathcal{D}v_t(\tau_w, r')/\mathcal{D}\tau_w}{r'(1 - \bar{\psi}(r'))(v_w + v_t(\tau_w, r'))^2} \int_0^{r'} \bar{\psi}(r'') r'' \, dr'' \, dr' \, dr, \quad (B8) \end{aligned}$$

where  $\mathcal{D}v_t(\tau_w, r')/\mathcal{D}\tau_w$  is obtained from (B5) as

$$\begin{aligned} \frac{\mathcal{D}v_t(\tau_w, r')}{\mathcal{D}\tau_w} = & (1 - \chi) \frac{\mathcal{D}v_{SIT}(\tau_w, r')}{\mathcal{D}\tau_w} + \chi \frac{\mathcal{D}v_{BIT}(\tau_w, r')}{\mathcal{D}\tau_w} \\ = & (1 - \chi) \left\{ \frac{1}{2} + \frac{R^+ - r'^+}{A^+} \frac{\exp(-(R^+ - r'^+)/A^+)}{(1 - \exp(-(R^+ - r'^+)/A^+))} \right\} \frac{v_{SIT}(\tau_w, r')}{\tau_w} \\ & + \chi \left\{ \frac{R^+ - r'^+}{A^+} \frac{\exp(-(R^+ - r'^+)/A^+)}{(1 - \exp(-(R^+ - r'^+)/A^+))} \right\} \frac{v_{BIT}(\tau_w, r')}{\tau_w}. \quad (B9) \end{aligned}$$

Table 4 shows the cases considered by the present simulation, Inoue *et al.* (1976), Sato *et al.* (1981b), Malnes (1966) and Liu (1997) for testing the present algebraic model. The

Case	$D$ (mm)	$d_{eq}$ (mm)	$\langle \psi \rangle$ (%)	$Re_{bulk}$	$Re_{bub}$	$\tau_w^*$ (Pa)	$\chi$	Remark
1		2.62	1.50		533	0.262	0.838	
2		3.30	1.50		737	0.205	0.828	
3	40	4.16	1.50	5300	1000	0.165	0.820	From present simulation
4		3.30	0.75		740	0.175	0.828	
5		3.30	3.00		724	0.261	0.828	
6	40	3.5	15	18 800	868	10.87	0.580	From Inoue <i>et al.</i> (1976)
7		4.4	7.1	17 500	1039	1.65	0.442	
8	26	4.8	13.1	18 700	1111	2.14	0.410	From Sato <i>et al.</i> (1981 <i>b</i> )
9		5.6	22.2	29 200	1280	4.43	0.295	
10		4.6	17.3	39 300	1074	6.46	0.157	
11	46	3	26	116 000	782	9.52	0.062	From Malnes (1966)
12		4.36	5.1	135 000	1033	10.99	0.041	
13		3.09	5.7	136 000	798	11.59	0.053	
14	57.2	5.61	9.5	142 000	1283	11.42	0.031	From Liu (1997)
15		4.22	10.5	143 000	1008	12.45	0.035	
16		6.95	17.2	155 000	1609	11.95	0.024	
17		4.54	18.0	156 000	1064	14.46	0.024	

Table 4. Cases considered for the present algebraic RANS model. Parameters  $Re_{bub}$  and  $\tau_w^*$  in this table are from the present simulation, Inoue *et al.* (1976), Sato, Sadatomi & Sekoguchi (1981*b*), Malnes (1966) and Liu (1997). Fraction  $\chi$  is obtained by (B6).

terminal velocities ( $u_T$ ) of all the cases are obtained from the plot of  $d_{eq}$  versus  $u_T$  for a bubble in pure water in Clift *et al.* (2005), with which the computed  $\chi$  ranges from 0.024 to 0.838. Figure 25 shows the errors in the wall shear stress predicted by the present model and that of Sato *et al.* (1981*a*) for the data available from the present simulation and previous experiments (Malnes 1966; Inoue *et al.* 1976; Sato *et al.* 1981*b*; Liu 1997). The solutions by the model of Sato *et al.* (1981*a*) diverged for cases 3 and 5, and thus they are marked as an error of  $-100\%$  in this figure. As shown, the model by Sato *et al.* (1981*a*) underestimates and overestimates the wall shear stresses at low and high water bulk Reynolds numbers, respectively. This is because the model constant used in Sato *et al.* (1981*a*) was determined based on the data at intermediate Reynolds numbers, and thus the predictions worked well at these Reynolds numbers. However, the present model predicts the wall shear stresses quite well for all the cases except case 6 (Inoue *et al.* 1976) and has overall a better prediction capability than the model by Sato *et al.* (1981*a*). Currently, we do not know why the prediction for case 6 is very different from the experimental result.

Figure 26 shows the mean axial water velocities predicted by the present model and that of Sato *et al.* (1981*a*) for the present simulation and previous experimental data. For cases 6, 8 and 11 ( $Re_{bulk} = 18\,800, 18\,700, 116\,000$ , respectively), the predictions of the mean axial velocities by both the present model and that of Sato *et al.* (1981*a*) agree well with the experimental data. However, for cases 1, 2 and 4 ( $Re_{bulk} = 5300$ ), the present model accurately predicts the mean axial velocities, while the model of Sato *et al.* (1981*a*) provides M-shaped velocity profiles which are very different from the simulation data.

The present algebraic model shows a better performance than the previous one at a wide range of the water bulk Reynolds number. However, the present model still requires the radial distribution of mean bubble volume fraction *a priori*, and thus the model itself is not stand-alone. Many RANS models including one-equation, two-equation and Reynolds stress models (Vaidheeswaran & Hibiki 2017) do not properly include the effect of the interaction between the shear-induced and bubble-induced turbulence. Therefore,

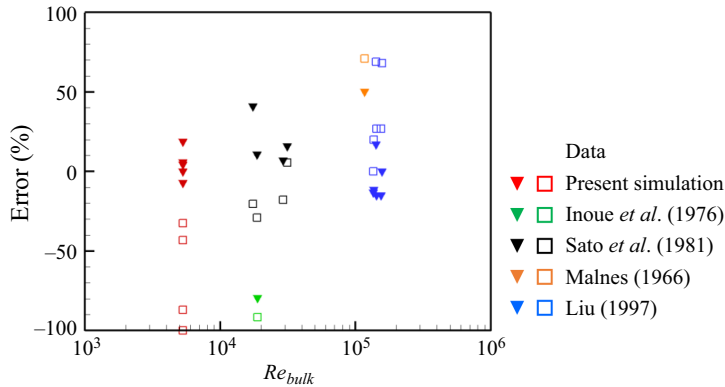


Figure 25. Error in the wall shear stress predicted by the RANS models of the present study (▼) and Sato *et al.* (1981b) (□). Here, the error is defined as  $(\tau_{w,RANS} - \tau_w^*)/\tau_w^* \times 100$ , where  $\tau_w^*$  is given in table 4.

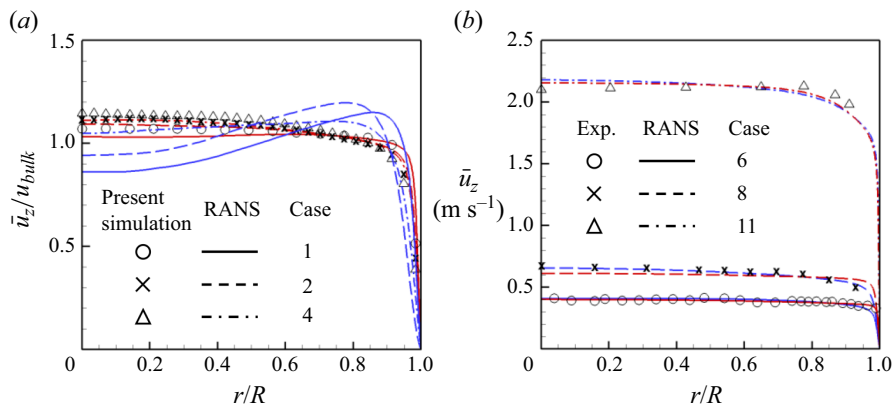


Figure 26. Mean axial water velocities predicted by the present model (red lines) and model by Sato *et al.* (1981a) (blue lines): (a) present simulation; (b) experiments (Malnes 1966; Inoue *et al.* 1976; Sato *et al.* 1981b). Here, the lines and symbols are from the algebraic RANS models and simulation/experimental data, respectively.

the approach adopted in the present model may be applied to a more general RANS model to improve its prediction capability for two-phase flows.

## REFERENCES

- ADOUA, R., LEGENDRE, D. & MAGNAUDET, J. 2009 Reversal of the lift force on an oblate bubble in a weakly viscous linear shear flow. *J. Fluid Mech.* **628**, 23–41.
- ALBADAWI, A., DONOGHUE, D.B., ROBINSON, A.J., MURRAY, D.B. & DELAURÉ, Y.M.C. 2014 On the assessment of a vof based compressive interface capturing scheme for the analysis of bubble impact on and bounce from a flat horizontal surface. *Intl J. Multiphase Flow* **65**, 82–97.
- ALMÉRAS, E., MATHAI, V., LOHSE, D. & SUN, C. 2017 Experimental investigation of the turbulence induced by a bubble swarm rising within incident turbulence. *J. Fluid Mech.* **825**, 1091–1112.
- AMOURA, Z., BESNACI, C., RISSO, F. & ROIG, V. 2017 Velocity fluctuations generated by the flow through a random array of spheres: a model of bubble-induced agitation. *J. Fluid Mech.* **823**, 592–616.
- BOIS, G. 2017 Direct numerical simulation of a turbulent bubbly flow in a vertical channel: towards an improved second-order reynolds stress model. *Nucl. Engng Des.* **321**, 92–103.
- BRACKBILL, J.U., KOTHE, D.B. & ZEMACH, C. 1992 A continuum method for modeling surface tension. *J. Comput. Phys.* **100** (2), 335–354.

- BRÜCKER, C. 1999 Structure and dynamics of the wake of bubbles and its relevance for bubble interaction. *Phys. Fluids* **11** (7), 1781–1796.
- CANO-LOZANO, J.C., MARTINEZ-BAZAN, C., MAGNAUDET, J. & TCHOUFAG, J. 2016 Paths and wakes of deformable nearly spheroidal rising bubbles close to the transition to path instability. *Phys. Rev. Fluids* **1** (5), 053604.
- CLIFT, R., GRACE, J.R. & WEBER, M.E. 2005 *Bubbles, Drops, and Particles*. Courier Corporation.
- COLIN, C., FABRE, J. & KAMP, A. 2012 Turbulent bubbly flow in pipe under gravity and microgravity conditions. *J. Fluid Mech.* **711**, 469–515.
- COLOMBO, M. & FAIRWEATHER, M. 2015 Multiphase turbulence in bubbly flows: RANS simulations. *Intl J. Multiphase Flow* **77**, 222–243.
- COYAJEE, E. & BOERSMA, B.J. 2009 Numerical simulation of drop impact on a liquid–liquid interface with a multiple marker front-capturing method. *J. Comput. Phys.* **228** (12), 4444–4467.
- DABIRI, S., LU, J. & TRYGGVASON, G. 2013 Transition between regimes of a vertical channel bubbly upflow due to bubble deformability. *Phys. Fluids* **25** (10), 102110.
- DE VRIES, A.W.G., BIESHEUVEL, A. & VAN WIJNGAARDEN, L. 2002 Notes on the path and wake of a gas bubble rising in pure water. *Intl J. Multiphase Flow* **28** (11), 1823–1835.
- VAN DRIEST, E.R. 1956 On turbulent flow near a wall. *J. Aeronaut. Sci.* **23** (11), 1007–1011.
- DU CLUZEAU, A., BOIS, G., LEONI, N. & TOUTANT, A. 2022 Analysis and modeling of bubble-induced agitation from direct numerical simulation of homogeneous bubbly flows. *Phys. Rev. Fluids* **7** (4), 044604.
- DU CLUZEAU, A., BOIS, G. & TOUTANT, A. 2019 Analysis and modelling of Reynolds stresses in turbulent bubbly up-flows from direct numerical simulations. *J. Fluid Mech.* **866**, 132–168.
- EGGELS, J.G., UNGER, F., WEISS, M.H., WESTERWEEL, J., ADRIAN, R.J., FRIEDRICH, R. & NIEUWSTADT, F.T. 1994 Fully developed turbulent pipe flow: a comparison between direct numerical simulation and experiment. *J. Fluid Mech.* **268**, 175–210.
- GOTTLIEB, S. & SHU, C.W. 1998 Total variation diminishing Runge–Kutta schemes. *Math. Comput.* **67** (221), 73–85.
- HERRMANN, M. 2008 A balanced force refined level set grid method for two-phase flows on unstructured flow solver grids. *J. Comput. Phys.* **227** (4), 2674–2706.
- HIBIKI, T. & ISHII, M. 2002 Interfacial area concentration of bubbly flow systems. *Chem. Engng Sci.* **57** (18), 3967–3977.
- INNOCENTI, A., JACCOD, A., POPINET, S. & CHIBBARO, S. 2021 Direct numerical simulation of bubble-induced turbulence. *J. Fluid Mech.* **918**, A23.
- INOUE, A., AOKI, S., KOGA, T. & YAEHASHI, H. 1976 Void fraction, bubble and liquid velocity profiles of two-phase bubble flow in a vertical pipe. *Trans. JSME* **42** (360), 2521–2531.
- JEONG, J. & HUSSAIN, F. 1995 On the identification of a vortex. *J. Fluid Mech.* **285**, 69–94.
- JIANG, G.S. & PENG, D. 2000 Weighted ENO schemes for Hamilton–Jacobi equations. *SIAM J. Sci. Comput.* **21** (6), 2126–2143.
- KATAOKA, I. 1995 Modeling and prediction of turbulence in bubbly two-phase flow. In *Proceedings of the 2nd International Conference on Multiphase Flow*, Kyoto, Japan, 3–7 April, vol. 2.
- KATAOKA, I. & SERIZAWA, A. 1989 Basic equations of turbulence in gas-liquid two-phase flow. *Intl J. Multiphase Flow* **15** (5), 843–855.
- KIM, D. 2011 Direct numerical simulation of two-phase flow with application to air layer drag reduction. PhD thesis, Stanford University.
- KIM, K. & CHOI, H. 2018 Direct numerical simulation of a turbulent core-annular flow with water-lubricated high viscosity oil in a vertical pipe. *J. Fluid Mech.* **849**, 419–447.
- KIM, M., LEE, J.H. & PARK, H. 2016 Study of bubble-induced turbulence in upward laminar bubbly pipe flows measured with a two-phase particle image velocimetry. *Exp. Fluids* **57**, 1–21.
- KREPPER, E., LUCAS, D. & PRASSER, H.M. 2005 On the modelling of bubbly flow in vertical pipes. *Nucl. Engng Des.* **235** (5), 597–611.
- LEE, J. & PARK, H. 2017 Wake structures behind an oscillating bubble rising close to a vertical wall. *Intl J. Multiphase Flow* **91**, 225–242.
- LEE, J.H., KIM, H., LEE, J. & PARK, H. 2021 Scale-wise analysis of upward turbulent bubbly flows: an experimental study. *Phys. Fluids* **33** (5), 053316.
- LIAO, Y., RZEHAK, R., LUCAS, D. & KREPPER, E. 2015 Baseline closure model for dispersed bubbly flow: bubble coalescence and breakup. *Chem. Engng Sci.* **122**, 336–349.
- LIU, T.J. 1997 Investigation of the wall shear stress in vertical bubbly flow under different bubble size conditions. *Intl J. Multiphase Flow* **23** (6), 1085–1109.
- LIU, T.J. & BANKOFF, S.G. 1993 Structure of air-water bubbly flow in a vertical pipe–II. Void fraction, bubble velocity and bubble size distribution. *Intl J. Heat Mass Transfer* **36** (4), 1061–1072.



- LU, J. & TRYGGVASON, G. 2008 Effect of bubble deformability in turbulent bubbly upflow in a vertical channel. *Phys. Fluids* **20** (4), 040701.
- LU, J. & TRYGGVASON, G. 2013 Dynamics of nearly spherical bubbles in a turbulent channel upflow. *J. Fluid Mech.* **732**, 166–189.
- LUCAS, D., KREPPER, E. & PRASSER, H.M. 2001 Prediction of radial gas profiles in vertical pipe flow on the basis of bubble size distribution. *Intl J. Therm. Sci.* **40** (3), 217–225.
- LUCAS, D., KREPPER, E. & PRASSER, H.M. 2007 Use of models for lift, wall and turbulent dispersion forces acting on bubbles for poly-disperse flows. *Chem. Engng Sci.* **62** (15), 4146–4157.
- MA, T., SANTARELLI, C., ZIEGENHEIN, T., LUCAS, D. & FRÖHLICH, J. 2017 Direct numerical simulation–based Reynolds-averaged closure for bubble-induced turbulence. *Phys. Rev. Fluids* **2** (3), 034301.
- MALNES, D. 1966 Slip ratios and friction factors in the bubble flow regime in vertical tubes. *Tech. Rep.* KR-110. Institutt for Atomenergi.
- MARTÍNEZ-MERCADO, J., PALACIOS-MORALES, C.A. & ZENIT, R. 2007 Measurement of pseudoturbulence intensity in monodispersed bubbly liquids for  $10 < Re < 500$ . *Phys. Fluids* **19** (10), 103302.
- MENTER, F.R. 1994 Two-equation eddy-viscosity turbulence models for engineering applications. *AIAA J.* **32** (8), 1598–1605.
- MOURSALI, E., MARIÉ, J. & BATAILLE, J. 1995 An upward turbulent bubbly boundary layer along a vertical flat plate. *Intl J. Multiphase Flow* **21** (1), 107–117.
- PANDEY, V., RAMADUGU, R. & PERLEKAR, P. 2020 Liquid velocity fluctuations and energy spectra in three-dimensional buoyancy-driven bubbly flows. *J. Fluid Mech.* **884**, R6.
- PENG, D., MERRIMAN, B., OSHER, S., ZHAO, H. & KANG, M. 1999 A PDE-based fast local level set method. *J. Comput. Phys.* **155** (2), 410–438.
- VAN DER PIJL, S.P., SEGAL, A., VUIK, C. & WESSELING, P. 2005 A mass-conserving level-set method for modelling of multi-phase flows. *Intl J. Numer. Meth. Fluids* **47** (4), 339–361.
- PRAKASH, V.N., MERCADO, J.M., VAN WIJNGAARDEN, L., MANCILLA, E., TAGAWA, Y., LOHSE, D. & SUN, C. 2016 Energy spectra in turbulent bubbly flows. *J. Fluid Mech.* **791**, 174–190.
- PROSPERETTI, A. 2002 *Drop-Surface Interactions*. Springer.
- RAESSI, M. & PITSCH, H. 2012 Consistent mass and momentum transport for simulating incompressible interfacial flows with large density ratios using the level set method. *Comput. Sci.* **63**, 70–81.
- RAYMOND, F. & ROSANT, J.M. 2000 A numerical and experimental study of the terminal velocity and shape of bubbles in viscous liquids. *Chem. Engng Sci.* **55** (5), 943–955.
- RIBOUX, G., LEGENDRE, D. & RISSO, F. 2013 A model of bubble-induced turbulence based on large-scale wake interactions. *J. Fluid Mech.* **719**, 362–387.
- RIBOUX, G., RISSO, F. & LEGENDRE, D. 2010 Experimental characterization of the agitation generated by bubbles rising at high Reynolds number. *J. Fluid Mech.* **643**, 509–539.
- RISSO, F. & ELLINGSEN, K. 2002 Velocity fluctuations in a homogeneous dilute dispersion of high-Reynolds-number rising bubbles. *J. Fluid Mech.* **453**, 395–410.
- ROGHAIR, I., MERCADO, J.M., ANNALAND, M.V.S., KUIPERS, H., SUN, C. & LOHSE, D. 2011 Energy spectra and bubble velocity distributions in pseudo-turbulence: numerical simulations vs experiments. *Intl J. Multiphase Flow* **37** (9), 1093–1098.
- ROIG, V. & DE TOURNEMINE, A.L. 2007 Measurement of interstitial velocity of homogeneous bubbly flows at low to moderate void fraction. *J. Fluid Mech.* **572**, 87–110.
- RZEHA, R. & KREPPER, E. 2013 CFD modeling of bubble-induced turbulence. *Intl J. Multiphase Flow* **55**, 138–155.
- SAFFMAN, P.G. 1965 The lift on a small sphere in a slow shear flow. *J. Fluid Mech.* **22** (2), 385–400.
- SANADA, T., SATO, A., SHIROTA, M. & WATANABE, M. 2009 Motion and coalescence of a pair of bubbles rising side by side. *Chem. Engng Sci.* **64** (11), 2659–2671.
- SATO, Y., SADATOMI, M. & SEKOGUCHI, K. 1981a Momentum and heat transfer in two-phase bubble flow—I. Theory. *Intl J. Multiphase Flow* **7** (2), 167–177.
- SATO, Y., SADATOMI, M. & SEKOGUCHI, K. 1981b Momentum and heat transfer in two-phase bubble flow—II. A comparison between experimental data and theoretical calculations. *Intl J. Multiphase Flow* **7** (2), 179–190.
- SEKOGUCHI, K., SATO, Y. & HONDA, T. 1974 An experimental investigation on bubble flow. *Trans. Japan Soc. Mech. Engng* **40**, 1395–1403.
- SON, G. 2001 A numerical method for bubble motion with phase change. *Numer. Heat Transfer B* **39** (5), 509–523.
- SPALART, P. & ALLMARAS, S. 1992 A one-equation turbulence model for aerodynamic flows. In *Proceedings of the 30th Aerospace Sciences Meeting and Exhibit*, p. 439. AIAA.

- SPEZIALE, C.G., SARKAR, S. & GATSKI, T.B. 1991 Modelling the pressure–strain correlation of turbulence: an invariant dynamical systems approach. *J. Fluid Mech.* **227**, 245–272.
- SUSSMAN, M., SMERKA, P. & OSHER, S. 1994 A level set approach for computing solutions to incompressible two-phase flow. *J. Comput. Phys.* **114** (1), 146–159.
- TANAKA, M. 2011 Numerical study on flow structures and heat transfer characteristics of turbulent bubbly upflow in a vertical channel. *Computational Simulations and Applications*. **20** (1), 119–142.
- TATEBE, O. 1993 The multigrid preconditioned conjugate gradient method. In *Proceedings of the Sixth Copper Mountain Conference on Multigrid Methods*, NASA, pp. 621–634. Copper Mountain.
- TOMIYAMA, A., TAMAI, H., ZUN, I. & HOSOKAWA, S. 2002 Transverse migration of single bubbles in simple shear flows. *Chem. Engng Sci.* **57** (11), 1849–1858.
- VAIDHEESWARAN, A. & HIBIKI, T. 2017 Bubble-induced turbulence modeling for vertical bubbly flows. *Intl J. Heat Mass Transfer* **115**, 741–752.
- WANG, S.K.L. 1986 *Three-Dimensional Turbulence Structure Measurements in Air/Water Two-Phase Flow (Hot-Film Anemometer, Reynolds Stresses, Void Fraction)*. Rensselaer Polytechnic Institute.
- WHITE, F.M. 1979 *Fluid Mechanics*. McGraw-Hill Education.
- WU, X. & MOIN, P. 2009 Direct numerical simulation of turbulence in a nominally zero-pressure-gradient flat-plate boundary layer. *J. Fluid Mech.* **630**, 5–41.
- YAN, H., ZHANG, H., LIAO, Y., ZHANG, H., ZHOU, P. & LIU, L. 2022 A single bubble rising in the vicinity of a vertical wall: a numerical study based on volume of fluid method. *Ocean Engng* **263**, 112379.
- YANG, J. & BALARAS, E. 2006 An embedded-boundary formulation for large-eddy simulation of turbulent flows interacting with moving boundaries. *J. Comput. Phys.* **215** (1), 12–40.
- ZHANG, H., YOKOMINE, T. & KUNUGI, T. 2015 Turbulence modulation of the upward turbulent bubbly flow in vertical ducts. *Nucl. Engng Technol.* **47** (5), 513–522.
- ZHANG, J., NI, M.J. & MAGNAUDET, J. 2021 Three-dimensional dynamics of a pair of deformable bubbles rising initially in line. Part 1. Moderately inertial regimes. *J. Fluid Mech.* **920**, A16.
- ZHANG, J., NI, M.J. & MAGNAUDET, J. 2022 Three-dimensional dynamics of a pair of deformable bubbles rising initially in line. Part 2. Highly inertial regimes. *J. Fluid Mech.* **943**, A10.
- ZHANG, Y., ZOU, Q., GREAVES, D., REEVE, D., HUNT-RABY, A., GRAHAM, D., JAMES, P. & LV, X. 2010 A level set immersed boundary method for water entry and exit. *Commun. Comput. Phys.* **8** (2), 265–288.